AIMS Mathematics

http://www.aimspress.com/journal/Math

AIMS Mathematics, 11(6): 19088–19126.
DOI: 10.3934/math.2026778
Received: 15 April 2026
Revised: 02 June 2026
Accepted: 15 June 2026
Published: 29 June 2026

Research article

Distributed finite-time coordination and tracking control for partially shaded photovoltaic arrays

Omar Kahouli[1,*], Sulaiman Almohaimeed[2,*], Lilia El Amraoui[3], Mohamed Ayari[4,*] and Omar Naifar[5,6]

[1] Department of Electronics Engineering, Applied College, University of Ha'il, Ha'il 2440, Saudi Arabia

[2] Department of Electrical Engineering, College of Engineering, Qassim University, 52571, Saudi Arabia

[3] Department of Electrical Engineering, College of Engineering, Princess Nourah bint Abdulrahman University, P.O. Box 84428, Riyadh 11671, Saudi Arabia

[4] Department of Information Technology, Faculty of Computing and Information Technology, Northern Border University, Arar 91431, Saudi Arabia

[5] Higher Institute of Applied Sciences and Technology of Kairouan, University of Kairouan, Kairouan, Tunisia

[6] Control and Energy Management Laboratory, National School of Engineering of Sfax, Sfax University, Sfax, Tunisia

* **Correspondence:** Email: omarkahouli@yahoo.fr, sulaiman.m@qu.edu.sa, mohamed.ayari@nbu.edu.sa.

Abstract: This paper proposes a distributed finite-time coordination and tracking control framework for partially shaded photovoltaic (PV) arrays. The considered architecture combines a sampled-data outer coordination layer with a continuous-time inner tracking layer in order to improve global power extraction under nonuniform irradiance conditions. At the local level, each PV submodule is equipped with an artificial neural network (ANN) that provides a fast estimate of a baseline operating voltage from irradiance and temperature measurements. To move beyond purely local maximum power point tracking (MPPT) operation, a distributed finite-time observer is developed so that every agent reconstructs the sampled total array power using only neighbor-to-neighbor communication. Based on this shared information, a cooperative projected-ascent command-update law is introduced to refine the ANN initialization and generate improved voltage commands through a regularized sampled objective. In the inner loop, a reference filter and a robust sliding-mode controller are designed to guarantee accurate voltage tracking despite bounded modeling uncertainty and disturbances. Theoretical outputs determine the possibility of finite-time recovery of the sampled total power, the monotonicity and stationarity of the distributed command-update law, and the finite-time convergence to the sliding manifold and exponential tracking of the filtered command. Simulation studies carried out on a four-agent partially shaded PV array confirm the effectiveness of the proposed framework. Specifically, the distributed observer converges within the prescribed coordination interval, the cooperative outer layer monotonically improves the sampled cooperative objective, and the overall closed-loop architecture delivers an average power gain of 13.4079% across the tested irradiance scenarios. These findings indicate that the proposed distributed architecture provides a flexible and reliable solution for cooperative MPPT in partially shaded PV systems.

Keywords: photovoltaic systems; partial shading; maximum power point tracking; distributed control; finite-time observer; projected ascent; sliding mode control; artificial neural networks; multi-agent systems; cooperative optimization

Mathematics Subject Classification: 93C10, 93C42, 93D09, 93D05, 68T07, 49M37, 91A24

1. Introduction

Photovoltaic (PV) generation is now a key component of modern low-carbon energy systems, and its practical efficiency depends on the ability to operate close to the maximum power point under rapidly changing environmental conditions. Under partial shading conditions (PSCs), the mismatch between irradiated modules produces multiple local maxima in the aggregate power–voltage characteristic so that conventional local search techniques may settle on suboptimal operating points. Maximum power point tracking (MPPT) under PSCs has therefore attracted continuous interest in the literature. Early model-predictive overviews [1] and, more recently, comprehensive surveys [2–4] highlight both the wealth of available approaches and the persistent gap between local tracking performance and global power extraction under nonuniform irradiance.

PV systems have been studied with a wide range of MPPT techniques. Discrete model predictive control and other model-based methods such as discrete model predictive control can enhance dynamic response and constraint management; however, they presuppose the availability of appropriate models and can be computationally intensive in large-scale applications [1]. These have led to the development of data-driven and intelligent MPPT methods that are also appealing in nonlinear and uncertain operating conditions. MPPT schemes based on ANNs have been shown to exhibit rapid adaptation to changing shading conditions, and they can be applied to predict operating points based on measurements of the environment [5, 6]. Hybrid intelligent methods founded on the adaptive neuro-fuzzy inference system (ANFIS), particle swarm optimization, and predictive fuzzy dynamic programming have more recently been suggested to enhance robustness, convergence speed, and power extraction ability in grid-connected or hybrid PV systems [7–9]. Related intelligent and optimization-based control techniques for power systems, including fuzzy-logic, genetic-algorithm, and FACTS-based approaches, provide complementary methodologies [10–12]. Similarly, metaheuristic and evolutionary models, such as genetic algorithm-based MPPT, have been found to promise benefits in escaping local extrema under PSCs [13]. Most intelligent MPPT strategies, however, are fundamentally local in nature: They rely on local measurements or estimators of individual modules and do not explicitly impose cooperative optimization over a network of interconnected PV submodules.

Alongside controller design, an equal research line has been investigating the reduction of PSC effects on arrays by electrical reconfigurability, array layout, and structural design. Recent studies have proposed new array layout techniques, simplified physical rearrangements of strings, and pandiagonal magic square layouts to maximize energy recovery in the presence of shading [14–16], together with adaptive battery-based reconfiguration schemes and improved optimization processes [17, 18]. Other publications have explored specific maximum power estimation algorithms of partially shaded arrays and discussed wide-based mitigation techniques, such as the importance of bypass diode design and advanced interconnection techniques [19–21]. Although these methods can enhance the power performance that the tracker observes, they alone fail to solve the critical control issue that is the focus of this paper: How to implement a scalable and high-performance distributed controller that coordinates many converter-interfaced PV units and orient the overall array to a high-performance operating point when faced with nonuniform irradiance.

The necessity is a natural incentive to the application of the concept of distributed control. Covering related fields, cooperative distributed algorithms have been used in practice to restore voltage and frequency in microgrids that use inverters, coordinate reactive power in PV-rich systems, and adaptive event-driven regulation in islanded AC microgrids [22–24]. Closely related to the sampled-data outer layer used in the present work, event-triggered control has been investigated for digital MPPT implementation and for PV-rich microgrids in order to reduce their communication and computational burden while preserving stability [24, 25]. Theoretically, consensus-based control and finite-/fixed-time multi-agent coordination give powerful means to reach an agreement and information fusion with certain transient characteristics [26, 27]. Nevertheless, they are not the specific methods that have been designed to address the MPPT problem of partially shaded PV arrays, where the aim is not to agree on the same voltages but to work together in a distributed manner to achieve a command profile that maximizes the aggregate harvested power and take into consideration the nonhomogeneous local irradiance and temperature environments. Moreover, the existence of practical PV converters also necessitates high-speed and rugged low-level regulation that has the ability to follow ordered voltage trajectories in the presence of uncertainty in the models and external perturbations.

In the case of the inner tracking layer, sliding mode control is one of the most effective robust design paradigms of uncertain electromechanical and power-electronic systems due to its invariance properties, high disturbance rejection, and ability to reach a finite time [28, 29]. Simultaneously, recent advances in observer and convergence analysis, such as adaptive observers with fixed-time convergence, online disturbance learning, and fractional-order observer constructions of nonlinear systems, exemplify the present day interest in fast estimation, robustness, and low conservatism together in uncertain dynamical systems [30, 31]. These advances imply that an effective distributed MPPT architecture to operate PSC should combine three ingredients in a coherent fashion: (i) a rapid local predictor that can deliver a good initial guess of the operating point, (ii) a distributed coordination mechanism that can rebuild or utilize global performance information with only neighbor-to-neighbor communication, and (iii) a robust continuous-time tracking controller that can enforce the commanded operating voltages at the converter level.

Motivated by the above observations, this paper proposes a distributed finite-time coordination and tracking control framework for partially shaded photovoltaic arrays. The proposed architecture integrates local ANN-based estimation, cooperative sampled-data optimization, and robust inner-loop tracking. Each PV submodule is equipped with a local ANN that predicts a baseline MPP voltage from irradiance and temperature measurements. These local predictions are not used as final commands; instead, they serve as the initialization of a distributed outer-loop coordination scheme in which the agents exchange information with their neighbors and collectively refine their voltage commands. A finite-time distributed observer reconstructs the sampled total array power using only neighbor-to-neighbor communication, providing every agent with a common global performance indicator without centralized measurement. Building on this shared information and on the locally sampled power maps, a distributed projected-ascent command-update law is formulated to optimize a cooperative sampled objective that balances harvested power, ANN regularization, and interagent coordination. Finally, because the outer coordination layer operates in sampled time, whereas the converter dynamics evolve in continuous time, a robust sliding-mode tracking controller is combined with a filtered reference generator to ensure accurate voltage tracking in the presence of model uncertainty and bounded disturbances.

The contributions of this work are summarized as follows. First, a two-time-scale distributed architecture for MPPT under partial shading is developed, with an explicit interface between local ANN prediction, distributed finite-time power estimation, cooperative command generation, and continuous-time converter-level control. Second, a finite-time distributed observer is constructed so that every agent can reconstruct the sampled total array power via neighbor-to-neighbor communication only. Third, a projected-ascent outer-loop update is formulated and analyzed, ensuring monotonic improvement of a sampled cooperative objective and convergence to first-order stationary points under standard smoothness conditions. Fourth, a robust sliding-mode inner controller is designed that guarantees finite-time convergence to the sliding manifold and asymptotic tracking of the filtered command profile under bounded uncertainty. Together, these contributions deliver a mathematically consistent distributed control framework for cooperative power extraction under partial shading, going beyond both purely local MPPT and purely structural shading mitigation.

The remainder of the paper is organized as follows. Section 2 introduces the PV-array architecture, the communication graph, the local uncertain model, the ANN-based baseline predictor, and the reference generation mechanism. Section 3 presents the distributed finite-time power reconstruction scheme, the cooperative command update law, and the robust inner tracking controller, together with their theoretical guarantees. Section 4 reports the simulation results validating the observer, the outer coordination mechanism, and the tracking performance on representative partial shading scenarios. Section 5 concludes the paper.

2. Preliminaries

This section introduces the mathematical and architectural framework used throughout the paper. In order to address the cooperative nature of the partially shaded maximum power point tracking problem, we adopt a two-layer distributed structure:

- An *outer coordination layer*, updated at discrete coordination instants, whose role is to estimate global performance quantities and generate cooperative voltage commands;
- An *inner continuous-time tracking layer*, whose role is to force each PV submodule to follow the commanded voltage trajectory despite model uncertainty and external disturbances.

This decomposition is introduced here explicitly in order to connect the distributed estimation stage with the continuous-time controller and to clarify the role of the ANN-based local predictor in the overall architecture.

2.1. PV array architecture and local variables

Consider a photovoltaic (PV) generation system composed of N converter-interfaced PV submodules, indexed by

$$i \in \mathcal{V} = \{1, 2, \ldots, N\}.$$

Each agent i consists of the following:
- one PV panel or PV subarray,
- one dedicated DC–DC converter,
- one local digital controller,
- local sensors measuring the PV-side voltage $V_{p,i}$, current $I_{p,i}$, irradiance E_i, and temperature T_i.

The instantaneous electrical power generated by agent i is

$$P_i(t) = V_{p,i}(t) I_{p,i}(t), \tag{2.1}$$

and the total array power is

$$P_{\text{tot}}(t) = \sum_{i=1}^{N} P_i(t). \tag{2.2}$$

Under partial shading conditions, the irradiance profile is nonuniform, that is, $E_i(t) \neq E_j(t)$ in general. As a result, the aggregated power characteristic of the overall array may exhibit multiple local maxima. Therefore, optimizing each local power P_i independently does not generally maximize the global quantity P_{tot}, and a cooperative mechanism is required.

2.2. Two-time-scale distributed architecture

Figure 1 depicts the proposed two-time-scale distributed control architecture for a partially shaded photovoltaic array. The upper layer operates in discrete time and performs sampled-data coordination among neighboring agents. In this layer, each agent uses local measurements together with an ANN-based predictor to obtain a baseline estimate of the operating point near the maximum power point. The sampled local power is then exploited by a distributed finite-time observer to reconstruct an estimate of the total array power using only neighbor-to-neighbor information exchange. According to this estimate, the agents have a coordination variable that they update in a cooperative command update law, which might be thought of as a projected ascent step in conjunction with some consensuslike correction law. The bottom layer is continuous time and it is charged with the responsibility of correctly following the command sampled by the outer loop. The sampled coordination command is converted to smooth continuous reference by a reference generator or second-order filter, and an inner robust tracking controller is used to give finite-time convergence of the photovoltaic voltage trajectory despite model uncertainties and perturbations in the PV/converter dynamics. Comprehensively, the architecture decouples the systemwide coordination with fast local actuation, thus allowing scalable, communication-efficient, and robust distributed MPPT in the case of partial shading.

To formalize the interaction between estimation, coordination, and tracking, we introduce a sequence of coordination instants

$$0 = t_0 < t_1 < t_2 < \cdots, \qquad h_k := t_{k+1} - t_k > 0.$$

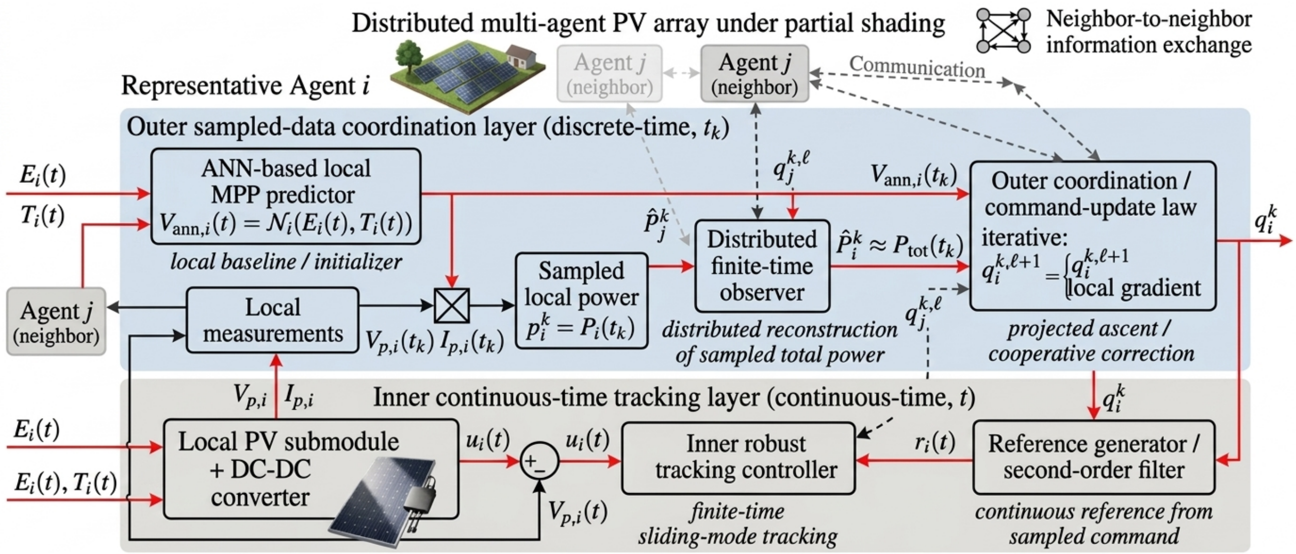

Figure 1. Overall two-time-scale distributed control architecture for a partially shaded photovoltaic array. Each agent integrates local measurements, ANN-based local maximum power point prediction, distributed finite-time power estimation, cooperative command generation, reference filtering, and robust inner-loop tracking control.

At each instant t_k, every agent performs the following operations:

1. It samples its local electrical power $P_i(t_k)$.
2. It exchanges information with its neighbors to estimate a global coordination variable, in particular the total sampled power.
3. It updates a local command variable q_i^k, which is used to generate a continuous reference trajectory $r_i(t)$ over the interval $[t_k, t_{k+1})$.

Hence, the discrete-time variables $\{q_i^k\}_{k\geq 0}$ belong to the outer coordination layer, whereas the continuous-time reference $r_i(t)$ belongs to the inner tracking layer.

2.3. *Control-oriented local model under uncertainty*

For control design purposes, each converter-interfaced PV submodule is described by a control-affine averaged model. Let $x_i \in \mathbb{R}^{n_i}$ denote the local state vector, $u_i \in \mathcal{U}_i \subset \mathbb{R}$ the control input (typically the converter duty cycle or an equivalent modulation signal), and $y_i = V_{p,i}$ the controlled output. We assume that the averaged subsystem dynamics can be written as

$$\dot{x}_i = f_i(x_i, E_i, T_i) + g_i(x_i, E_i, T_i)u_i + d_i(t), \qquad y_i = h_i(x_i) = V_{p,i}, \tag{2.3}$$

where $f_i(\cdot)$ and $g_i(\cdot)$ are locally Lipschitz vector fields, and $d_i(t)$ is a bounded disturbance term.

To facilitate sliding-mode design, we assume that the voltage output admits a relative-degree-two representation on the operating region of interest:

$$\ddot{V}_{p,i} = F_i(z_i, E_i, T_i, t) + B_i(z_i, E_i, T_i, t)u_i + \Delta_i(t), \tag{2.4}$$

where

$$z_i := [V_{p,i}, \dot{V}_{p,i}]^\top,$$

$F_i(\cdot)$ is a nonlinear drift term, $B_i(\cdot)$ is the input gain, and $\Delta_i(t)$ is a bounded disturbance.

However, in the subsequent control design, we do *not* assume exact knowledge of F_i and B_i. Instead, we introduce nominal locally Lipschitz functions $\hat{F}_i(\cdot)$ and $\hat{B}_i(\cdot)$ available to the controller and rewrite (2.4) as

$$\ddot{V}_{p,i} = \hat{F}_i(z_i, E_i, T_i, t) + \hat{B}_i(z_i, E_i, T_i, t)u_i + \varpi_i(z_i, E_i, T_i, u_i, t), \tag{2.5}$$

where the lumped uncertainty term is defined by

$$\varpi_i := (F_i - \hat{F}_i) + (B_i - \hat{B}_i)u_i + \Delta_i. \tag{2.6}$$

The decomposition (2.5)–(2.6) explicitly accounts for modeling errors in both the drift and the input gain. It will allow the tracking controller to rely only on nominal quantities and known uncertainty bounds rather than on exact model cancellation.

2.4. Local ANN-based MPP prediction and its role

Each agent is equipped with a pretrained artificial neural network (ANN) that provides a fast estimate of its *local* maximum power point (MPP) voltage using only its local environmental measurements:

$$V_{\text{ann},i}(t) = \mathcal{N}_i(E_i(t), T_i(t)), \tag{2.7}$$

where $\mathcal{N}_i(\cdot)$ denotes the ANN associated with agent i.

Let $V_{\text{mpp},i}(E_i, T_i)$ denote the true local MPP voltage under the local environmental conditions. The ANN estimation error is defined as

$$\varepsilon_i^{\text{ann}}(t) = V_{\text{ann},i}(t) - V_{\text{mpp},i}(E_i(t), T_i(t)). \tag{2.8}$$

The ANN output is not used as the final operating point of the distributed system. Instead, it plays the role of a *local initializer* or *baseline command* for the outer coordination layer. More precisely, the command update at time t_k will be constructed in the form

$$q_i^k = V_{\text{ann},i}(t_k) + \delta_i^k, \tag{2.9}$$

where δ_i^k is a cooperative correction term produced by the distributed coordination mechanism. Consequently, the ANN provides fast local adaptation, and the correction term δ_i^k accounts for the global coupling induced by partial shading.

ANN training details. Each network $\mathcal{N}_i(\cdot)$ is a shallow feedforward perceptron with two inputs (E_i, T_i), one hidden layer of 10 neurons with a hyperbolic-tangent activation, and a single linear output neuron returning $V_{\text{ann},i}$. The training dataset is generated off-line from the single-diode PV model of the considered submodule by sweeping the irradiance over $[100, 1100]\ \text{W/m}^2$ and the temperature over $[10, 55]\ ^\circ\text{C}$ and by extracting the corresponding numerical MPP voltage. The resulting dataset contains 2000 input/output samples and is randomly partitioned into 70% for training, 15% for validation, and 15% for testing. Training is performed with the Levenberg–Marquardt algorithm using early stopping on the validation set. The resulting performance on the held-out test set is reported in Table 1: Normalized RMSE $\approx 1.2\%$, MAE $\approx 0.9\%$, and coefficient of determination $R^2 \approx 0.998$. These figures justify the bounded-error assumption stated in Assumption 5.

Table 1. Per-agent ANN test-set performance after Levenberg–Marquardt training with early stopping.

Agent	RMSE (V)	MAE (V)	R^2
1	0.371	0.286	0.9985
2	0.388	0.301	0.9982
3	0.402	0.310	0.9979
4	0.395	0.305	0.9981

2.5. *Reference generation from discrete commands*

Because the outer coordination layer is updated only at the coordination instants t_k, although the inner tracking controller acts in continuous time, a reference generator is needed to convert the discrete command sequence $\{q_i^k\}$ into a sufficiently smooth trajectory $r_i(t)$.

For each agent i, we introduce the second-order reference filter

$$\ddot{r}_i + 2\zeta_i\omega_i\dot{r}_i + \omega_i^2 r_i = \omega_i^2 q_i^k, \qquad t \in [t_k, t_{k+1}), \tag{2.10}$$

where $\omega_i > 0$ and $\zeta_i > 0$ are design parameters, and q_i^k is held constant over the interval $[t_k, t_{k+1})$.

This filter ensures that the reference $r_i(t)$ is continuous and piecewise twice differentiable. Therefore, the inner sliding-mode tracking problem can be formulated with a regular reference signal even though the command updates are produced only at discrete times.

2.6. *Communication graph*

The information exchange among the N local controllers is modeled by an undirected graph

$$\mathcal{G} = (\mathcal{V}, \mathcal{E}),$$

where $\mathcal{V} = \{1, 2, \ldots, N\}$ is the node set, and $\mathcal{E} \subseteq \mathcal{V} \times \mathcal{V}$ is the edge set. If $(i, j) \in \mathcal{E}$, then agents i and j can exchange information.

Definition 2.1 (Adjacency matrix)**.** The adjacency matrix of $\mathcal{G}$ is $\boldsymbol{A} = [a_{ij}] \in \mathbb{R}^{N\times N}$, where

$$a_{ij} = \begin{cases} 1, & \text{if } (i, j) \in \mathcal{E}, \\ 0, & \text{otherwise.} \end{cases}$$

Because the graph is undirected, $a_{ij} = a_{ji}$.

Definition 2.2 (Degree matrix)**.** The degree matrix is the diagonal matrix $\boldsymbol{D} = \mathrm{diag}(d_1, \ldots, d_N)$, where

$$d_i = \sum_{j=1}^{N} a_{ij}.$$

Definition 2.3 (Laplacian matrix)**.** The graph Laplacian is defined as

$$\boldsymbol{L} = \boldsymbol{D} - \boldsymbol{A}. \tag{2.11}$$

Its entries satisfy

$$l_{ij} = \begin{cases} -a_{ij}, & i \neq j, \\ \sum_{k \neq i} a_{ik}, & i = j. \end{cases}$$

For an undirected connected graph, $\boldsymbol{L}$ is symmetric positive semidefinite, has a simple zero eigenvalue, and satisfies

$$\boldsymbol{L}\mathbf{1}_N = \mathbf{0}.$$

The graph is used for two purposes:

- Distributed reconstruction of global performance quantities such as the total sampled power;
- Distributed generation of the cooperative correction terms δ_i^k.

2.7. Cooperative optimization objective

The overall objective is to regulate the converter inputs u_i so that the total harvested power is maximized:

$$\max_{u_1,\dots,u_N} P_{\text{tot}}(t) = \max_{u_1,\dots,u_N} \sum_{i=1}^{N} P_i(V_{p,i}(t), I_{p,i}(t)), \tag{2.12}$$

subject to the local dynamics and input constraints.

Equivalently, in terms of the PV-side operating voltages, the cooperative objective can be written as

$$\max_{V_{p,1},\dots,V_{p,N}} \sum_{i=1}^{N} P_i(V_{p,i}; E_i, T_i). \tag{2.13}$$

Let

$$P_{\text{tot}}^{\star}(t) = \max_{V_{p,1},\dots,V_{p,N}} \sum_{i=1}^{N} P_i(V_{p,i}; E_i, T_i) \tag{2.14}$$

denote the maximum available power under the current operating conditions, and let

$$V_p^{\star}(t) = \left(V_{p,1}^{\star}(t), \dots, V_{p,N}^{\star}(t)\right)^{\top}$$

denote a corresponding optimal voltage profile.

In general, the components of $V_p^{\star}(t)$ need not be identical. Therefore, the term "distributed coordination" in this work refers to cooperation through exchanged information and coordinated command updates, not to the imposition of identical PV-side voltages.

2.8. Distributed estimation and command update objectives

No single agent is assumed to have direct access to $P_{\text{tot}}(t)$ or to the optimal profile $V_p^{\star}(t)$. Instead, each controller computes the following:

- A distributed estimate $\hat{P}_i^k$ of the total sampled power $P_{\text{tot}}(t_k)$;
- A command sample q_i^k, obtained by combining the local ANN prediction with a distributed correction term.

The estimation objective is

$$\hat{P}_i^k = P_{\mathrm{tot}}(t_k), \qquad \forall i \in \mathcal{V}, \tag{2.15}$$

after a sufficiently short estimation interval.

The coordination objective is to construct the correction terms δ_i^k in (2.9) using only local information, neighbor communication, ANN predictions, and distributed power estimates so that the resulting command sequence monotonically improves a sampled cooperative performance objective and converges to a first-order stationary point of the corresponding constrained optimization problem.

The continuous-time tracking objective is then

$$V_{p,i}(t) \to r_i(t) \qquad \text{for each } i \in \mathcal{V}, \tag{2.16}$$

where $r_i(t)$ is generated by the reference filter (2.10) from the command sequence q_i^k.

2.9. Standing assumptions

The subsequent analysis is based on the following assumptions.

Assumption 1 (Connected communication graph)**.** *The graph $\mathcal{G}$ is undirected and connected.*

Assumption 2 (Regularity of local dynamics)**.** *For each agent i, the functions $f_i(\cdot)$, $g_i(\cdot)$, $F_i(\cdot)$, $B_i(\cdot)$, $\hat{F}_i(\cdot)$, and $\hat{B}_i(\cdot)$ are locally Lipschitz in their arguments on the operating region of interest.*

Assumption 3 (Input gain bounds)**.** *There exist known constants $0 < \underline{B}_i \le \overline{B}_i$ such that*

$$0 < \underline{B}_i \le \hat{B}_i(z_i, E_i, T_i, t) \le \overline{B}_i$$

for all admissible trajectories and all $t \ge 0$.

Assumption 4 (Bounded lumped uncertainty)**.** *For each agent i, the lumped uncertainty ϖ_i defined in* (2.6) *is bounded on the operating region. That is, there exists a known constant $\bar{\varpi}_i > 0$ such that*

$$|\varpi_i(z_i, E_i, T_i, u_i, t)| \le \bar{\varpi}_i$$

for all admissible states, inputs, and times.

Assumption 5 (Bounded ANN estimation error)**.** *For each agent i, the ANN estimation error satisfies*

$$|\varepsilon_i^{\mathrm{ann}}(t)| \le \bar{\varepsilon}_i$$

for some finite constant $\bar{\varepsilon}_i > 0$.

Assumption 6 (Regularity of local power maps)**.** *For each agent i, the map*

$$V \mapsto P_i(V; E_i, T_i)$$

is continuously differentiable with respect to V on the operating interval of interest, and its derivative is locally Lipschitz uniformly with respect to bounded environmental conditions.

Assumption 7 (Regularity of the sampled cooperative objective)**.** *For each coordination instant t_k, the sampled cooperative objective introduced in Section 3 is continuously differentiable on the admissible command set $\mathcal{Q}$, and its gradient is Lipschitz continuous on $\mathcal{Q}$.*

Remark 2.4 (Validity of the Lipschitz-gradient assumption under PSCs). Although the aggregated power objective $J_k(q) = \sum_i P_i(q_i; E_i(t_k), T_i(t_k))$ is generically nonconcave under partial shading (Remark 2.6 below), Assumption 7 does not require concavity. It only asks that $\nabla\Psi_k$ be Lipschitz on the compact set $\mathcal{Q}$. For the single-diode PV model used here, the map $v \mapsto P_i(v; E_i, T_i)$ is smooth (C^∞) on the open feasible voltage range, so $(\phi_i^k)'$ is continuously differentiable and hence Lipschitz on the compact admissible interval $\mathcal{Q}_i$. The quadratic ANN-regularization and graph coupling terms in (3.11) contribute the constant Hessian $-\gamma I - \beta_c \boldsymbol{L}$, whose induced Lipschitz constant is exactly $\gamma + \beta_c \lambda_{\max}(\boldsymbol{L})$. A finite Lipschitz constant L_k is therefore guaranteed independently of the local concavity/convexity sign of the PV characteristic, and the constant $\gamma > 0$ only improves it. Combining the smoothness of ϕ_i^k on $\mathcal{Q}_i$ with the constant Hessian contributed by the regularization yields the explicit bound

$$L_k \;\leq\; \max_{i\in\mathcal{V}} \sup_{v\in\mathcal{Q}_i} \left|(\phi_i^k)''(v)\right| \;+\; \gamma \;+\; \beta_c\, \lambda_{\max}(\boldsymbol{L}), \tag{2.17}$$

which directly answers the concern about nonconvexity/nonconcavity: The first term captures the worst-case curvature of the local PV power maps over the compact admissible set, and the second and third terms are constants under the designer's control. This assumption is hence reasonable in the nonconvex/nonconcave PSC setting. When bypass-diode conduction is modeled, the characteristic $v \mapsto P_i(v; E_i, T_i)$ may exhibit isolated points of nondifferentiability at the diode switching voltages; in that case, Assumption 7 is enforced by working with a smoothed power map (e.g., a piecewise-cubic or tanh-based diode model) on the operating interval of interest, an approximation that is standard in PV simulation and that does not affect the qualitative conclusions of Theorem 3.6.

Assumption 8 (Slowly varying environmental signals)**.** *The irradiance and temperature signals $E_i(t)$ and $T_i(t)$ are bounded and piecewise continuously differentiable. Consequently, the local powers $P_i(t)$ and the global power $P_{\text{tot}}(t)$ are piecewise continuously differentiable and possess bounded time derivatives on compact intervals.*

Assumption 9 (Reference filter well-posedness)**.** *For each agent i, the command sequence $\{q_i^k\}_{k\geq 0}$ is bounded. Therefore, the reference generator* (2.10) *admits a unique bounded solution $r_i(t)$ such that r_i, $\dot{r}_i$, and $\ddot{r}_i$ are bounded on every compact interval.*

Remark 2.5. Assumption 5 does not mean that the ANN will find the global optimum. Only a local base prediction $V_{\text{ann},i}$ is added to the ANN, and the global coordination information is added by the distributed correction term δ_i^k.

Remark 2.6. The sampled cooperative optimization problem is typically nonconvex (or, in maximization form, nonconcave) due to the PV power characteristics, which can exhibit multiple local maxima in the partial shading regime. The outer coordination layer is, in turn, structured to ensure that, under typical smoothness conditions, it is monotone and converges to first-order stationary points; more stringent global optimality results require additional concavity conditions.

Remark 2.7. The addition of the command, q_i^k, and reference generator, (2.10), eliminates the uncertainty between the sampled outer-layer signal and the continuous-time reference needed by the inner controller. This decoupling is necessary to a mathematically consistent hybrid distributed control model.

Remark 2.8. The uncertainty description (2.5)–(2.6) is deliberately stated in lumped form so that the subsequent controller design does not rely on the exact cancellation of the unknown plant dynamics.

Remark 2.9. The present paper aims at a distributed architecture in which the observer, the command update mechanism, and the tracking controller are explicitly connected. The observer provides global information, the ANN provides a local initialization, and the cooperative correction term modifies this initialization to improve global power extraction.

3. Main results

This section develops the main results of the proposed distributed architecture. In accordance with the two-layer structure introduced in Section 2, the analysis is divided into the following layers:

- An *outer sampled-data coordination layer*, which reconstructs the total sampled power and updates the command sequence q_i^k;
- An *inner continuous-time tracking layer*, which forces the PV-side voltage $V_{p,i}$ to track the filtered reference $r_i(t)$ generated from q_i^k.

The first part provides the distributed information and the cooperative command update, whereas the second part guarantees robust tracking in the presence of bounded uncertainty. All differential equations involving the discontinuous function sign(·) are understood in the sense of Filippov.

3.1. Distributed finite-time reconstruction of the sampled total power

At each coordination instant t_k, every agent samples its local electrical power,

$$p_i^k := P_i(t_k). \tag{3.1}$$

During the short estimation interval $[t_k, t_k + T_o)$, the sampled values p_i^k are treated as constants. Each agent then initializes the auxiliary observer state

$$\xi_i(0) = p_i^k \tag{3.2}$$

and evolves it according to the finite-time consensus protocol

$$\dot{\xi}_i = -k_o \sum_{j=1}^{N} a_{ij} |\xi_i - \xi_j|^{\rho} \operatorname{sign}(\xi_i - \xi_j), \qquad 0 < \rho < 1, \tag{3.3}$$

where $k_o > 0$ is a design gain. At the end of the estimation interval, the distributed estimate of the total sampled power is defined by

$$\hat{P}_i^k := N\, \xi_i(T_o). \tag{3.4}$$

Theorem 3.1 (Finite-time distributed reconstruction of the sampled total power)**.** *Suppose Assumption 1 holds. Consider the observer dynamics* (3.3) *initialized by* (3.2). *Then, for each coordination instant t_k, the following statements hold:*

(i) The average of the states ξ_i is invariant;

(ii) All observer states reach consensus in finite time;

(iii) The consensus value is exactly the average of the sampled powers, namely

$$\xi_i(\tau) = \frac{1}{N} \sum_{j=1}^{N} p_j^k, \qquad \forall i \in \mathcal{V}, \quad \forall \tau \geq T_o,$$

provided that

$$T_o \geq \frac{2\, W_k(0)^{\frac{1-\rho}{2}}}{k_o(1-\rho)(2\lambda_2(\boldsymbol{L}))^{\frac{1+\rho}{2}}}, \tag{3.5}$$

where

$$W_k(0) := \frac{1}{2}\sum_{i=1}^{N}\left(p_i^k - \frac{1}{N}\sum_{j=1}^{N} p_j^k\right)^2.$$

Consequently,

$$\hat{P}_i^k = \sum_{j=1}^{N} p_j^k = P_{\text{tot}}(t_k), \qquad \forall i \in \mathcal{V}.$$

Proof. Fix a coordination instant t_k. Because the sampled powers p_i^k are constant over $[t_k, t_k + T_o)$, the observer dynamics are autonomous on that interval.

Define

$$\bar{\xi}(\tau) := \frac{1}{N}\sum_{i=1}^{N} \xi_i(\tau).$$

Differentiating and substituting (3.3) yields

$$\dot{\bar{\xi}} = -\frac{k_o}{N}\sum_{i=1}^{N}\sum_{j=1}^{N} a_{ij}|\xi_i - \xi_j|^{\rho}\,\mathrm{sign}(\xi_i - \xi_j).$$

Because the graph is undirected, $a_{ij} = a_{ji}$, and

$$|\xi_i - \xi_j|^{\rho}\,\mathrm{sign}(\xi_i - \xi_j) = -|\xi_j - \xi_i|^{\rho}\,\mathrm{sign}(\xi_j - \xi_i),$$

the terms cancel pairwise in the double sum, so

$$\dot{\bar{\xi}} = 0.$$

Therefore, $\bar{\xi}(\tau) = \bar{\xi}(0)$ for all $\tau \in [0, T_o)$. By the initialization (3.2),

$$\bar{\xi}(0) = \frac{1}{N}\sum_{i=1}^{N} p_i^k.$$

Thus, the average is invariant and equal to the average sampled power.

Introduce the disagreement vector

$$\tilde{\xi} := \xi - \bar{\xi}\,\mathbf{1}_N, \qquad \xi = [\xi_1, \ldots, \xi_N]^\top.$$

Because $\bar{\xi}$ is constant, $\dot{\tilde{\xi}} = \dot{\xi}$. Consider the Lyapunov function

$$W(\tau) := \frac{1}{2}\|\tilde{\xi}(\tau)\|_2^2. \tag{3.6}$$

Using $\mathbf{1}_N^\top\dot{\xi} = 0$, one has

$$\dot{W} = \tilde{\xi}^\top\dot{\tilde{\xi}} = \tilde{\xi}^\top\dot{\xi} = \xi^\top\dot{\xi}.$$

Substituting the observer dynamics yields

$$\dot{W} = -k_o\sum_{i=1}^{N}\xi_i\sum_{j=1}^{N}a_{ij}|\xi_i-\xi_j|^\rho\,\mathrm{sign}(\xi_i-\xi_j).$$

By symmetrization over the undirected graph,

$$\dot{W} = -\frac{k_o}{2}\sum_{i=1}^{N}\sum_{j=1}^{N}a_{ij}(\xi_i-\xi_j)|\xi_i-\xi_j|^\rho\,\mathrm{sign}(\xi_i-\xi_j).$$

Because

$$(\xi_i-\xi_j)\,\mathrm{sign}(\xi_i-\xi_j) = |\xi_i-\xi_j|,$$

it follows that

$$\dot{W} = -\frac{k_o}{2}\sum_{i=1}^{N}\sum_{j=1}^{N}a_{ij}|\xi_i-\xi_j|^{1+\rho}. \tag{3.7}$$

Let $\boldsymbol{B}$ be an incidence matrix of the connected graph $\mathcal{G}$, and define the edge-difference vector

$$\zeta := \boldsymbol{B}^\top\xi.$$

Each component of ζ corresponds to one edge difference $\xi_i-\xi_j$, and (3.7) can be rewritten as

$$\dot{W} = -k_o\|\zeta\|_{1+\rho}^{1+\rho}.$$

Because $1+\rho\in(1,2)$, norm monotonicity yields

$$\|\zeta\|_{1+\rho} \geq \|\zeta\|_2.$$

Hence,

$$\dot{W} \leq -k_o\|\zeta\|_2^{1+\rho}.$$

Now,

$$\|\zeta\|_2^2 = \xi^\top\boldsymbol{B}\boldsymbol{B}^\top\xi = \xi^\top\boldsymbol{L}\xi.$$

Because $\tilde{\xi}$ is orthogonal to $\mathbf{1}_N$ and $\boldsymbol{L}\mathbf{1}_N = \mathbf{0}$,

$$\xi^\top\boldsymbol{L}\xi = \tilde{\xi}^\top\boldsymbol{L}\tilde{\xi}.$$

Because the graph is connected, $\lambda_2(\boldsymbol{L}) > 0$, and therefore

$$\tilde{\xi}^\top\boldsymbol{L}\tilde{\xi} \geq \lambda_2(\boldsymbol{L})\|\tilde{\xi}\|_2^2 = 2\lambda_2(\boldsymbol{L})W.$$

Combining these inequalities gives

$$\dot{W} \leq -k_o(2\lambda_2(\boldsymbol{L})W)^{\frac{1+\rho}{2}}.$$

Thus,

$$\dot{W} \le -c_o W^{\beta}, \qquad c_o := k_o(2\lambda_2(\boldsymbol{L}))^{\frac{1+\rho}{2}}, \quad \beta := \frac{1+\rho}{2} \in (0,1). \tag{3.8}$$

Because $\beta \in (0,1)$, (3.8) is a standard finite-time inequality, for every interval on which $W(\tau) > 0$,

$$\frac{d}{d\tau} W^{1-\beta} = (1-\beta)W^{-\beta}\dot{W} \le -(1-\beta)c_o.$$

Integrating from 0 to τ yields

$$W(\tau)^{1-\beta} \le W(0)^{1-\beta} - (1-\beta)c_o\tau.$$

Therefore, $W(\tau)$ reaches zero no later than

$$T_o = \frac{W(0)^{1-\beta}}{(1-\beta)c_o} = \frac{2\,W(0)^{\frac{1-\rho}{2}}}{k_o(1-\rho)(2\lambda_2(\boldsymbol{L}))^{\frac{1+\rho}{2}}}.$$

Once $W(\tau) = 0$, one has $\tilde{\xi}(\tau) = 0$; hence, $\xi_1(\tau) = \cdots = \xi_N(\tau)$.

Because the average $\bar{\xi}$ is invariant, the consensus value must be equal to $\bar{\xi}(0)$, that is,

$$\xi_i(\tau) = \frac{1}{N}\sum_{j=1}^{N} p_j^k \qquad \text{for all } \tau \ge T_o.$$

Multiplying by N and using (3.4) gives

$$\hat{P}_i^k = N\xi_i(T_o) = \sum_{j=1}^{N} p_j^k = P_{\text{tot}}(t_k), \qquad \forall i \in \mathcal{V}.$$

The proof is complete. □

Remark 3.2. Theorem 3.1 provides each agent with an exact distributed copy of the sampled total power $P_{\text{tot}}(t_k)$. This global scalar does not by itself determine the optimal operating point, but it supplies a common performance indicator that is available to all agents without centralized measurement.

Remark 3.3 (Essential difference from existing finite-time consensus protocols). Classical finite-time consensus laws such as the position-driving rules of [26, 27] are designed to drive a vector of *state* variables to a common value, and the agreement value is governed by the initial *states*. Applying such protocols directly here would force the local voltages $V_{p,i}$ toward a common voltage, which is precisely *not* the desired behavior under partial shading, as the optimal MPP voltages of differently shaded submodules generally differ. The protocol (3.3) instead operates on an *auxiliary* variable ξ_i initialized at the *sampled power* p_i^k, and only this auxiliary variable is driven to consensus. The agents thus reach agreement on the average sampled power, and each PV-side voltage $V_{p,i}$ remains free to settle at its own command q_i^k. In other words, the observer reuses a known finite-time consensus mechanism but in a *state-augmentation* role: It disentangles power–information fusion from voltage coordination. This distinction is essential for cooperative MPPT under PSCs and is not addressed by existing consensus protocols.

3.2. Distributed command generation law

We now define the outer-layer rule that generates the command sequence from the ANN prediction, local power information, and neighboring commands. Let

$$Q_i := [V_i^{\min}, V_i^{\max}], \qquad Q := Q_1 \times \cdots \times Q_N.$$

At a fixed coordination instant t_k, define the sampled local power functions

$$\phi_i^k(v) := P_i(v; E_i(t_k), T_i(t_k)), \qquad v \in Q_i. \tag{3.9}$$

The corresponding sampled total-power objective is

$$J_k(q) := \sum_{i=1}^{N} \phi_i^k(q_i), \qquad q = [q_1, \ldots, q_N]^\top \in Q. \tag{3.10}$$

To incorporate the ANN baseline and a smooth distributed coordination term, define the cooperative sampled objective

$$\Psi_k(q) := J_k(q) - \frac{\gamma}{2}\|q - V_{\mathrm{ann}}^k\|_2^2 - \frac{\beta_c}{4}\sum_{i=1}^{N}\sum_{j=1}^{N} a_{ij}(q_i - q_j)^2, \tag{3.11}$$

where

$$V_{\mathrm{ann}}^k := [V_{\mathrm{ann},1}(t_k), \ldots, V_{\mathrm{ann},N}(t_k)]^\top,$$

$\gamma \geq 0$ weights the ANN regularization, and $\beta_c \geq 0$ weights the distributed coordination term.

For a frozen environment snapshot t_k, we allow an outer optimization loop indexed by $\ell = 0, 1, 2, \ldots$. The corresponding command vector is denoted by

$$q^{k,\ell} := [q_1^{k,\ell}, \ldots, q_N^{k,\ell}]^\top \in Q.$$

The componentwise gradient of Ψ_k is

$$g_{i,k}(q) := \frac{\partial \Psi_k}{\partial q_i}(q) = (\phi_i^k)'(q_i) - \gamma(q_i - V_{\mathrm{ann},i}(t_k)) - \beta_c \sum_{j=1}^{N} a_{ij}(q_i - q_j). \tag{3.12}$$

Accordingly, the projected ascent update is

$$q_i^{k,\ell+1} = \Pi_{Q_i}\Big(q_i^{k,\ell} + \alpha_k g_{i,k}(q^{k,\ell})\Big), \qquad i \in \mathcal{V}, \tag{3.13}$$

or, in vector form,

$$q^{k,\ell+1} = \Pi_Q\Big(q^{k,\ell} + \alpha_k \nabla\Psi_k(q^{k,\ell})\Big), \tag{3.14}$$

where Π_Q denotes the Euclidean projection onto Q, and $\alpha_k > 0$ is the step size associated with the kth frozen optimization problem.

The command actually transmitted to the reference filter over the interval $[t_k, t_{k+1})$ is taken as the terminal iterate of this outer loop and is denoted by

$$q^k := \lim_{\ell \to \infty} q^{k,\ell},$$

whenever the limit exists.

Remark 3.4. In implementation, the outer loop is not run for infinitely many iterations. Instead, it is stopped after a finite number of iterations or when the increment satisfies

$$\|q^{k,\ell+1} - q^{k,\ell}\|_2 \leq \varepsilon_{\mathrm{out}}$$

for a prescribed tolerance $\varepsilon_{\mathrm{out}} > 0$. The resulting iterate is then used as the transmitted command over the interval $[t_k, t_{k+1})$ and can be interpreted as a practical approximation of a first-order stationary point of the sampled cooperative optimization problem.

Remark 3.5. The update law (3.13) explicitly integrates the ANN through the term $V_{\mathrm{ann},i}(t_k)$, and it uses only local gradients and neighboring command values. The shared estimate $\hat{P}_i^k = P_{\mathrm{tot}}(t_k)$ obtained in Theorem 3.1 provides a common distributed record of the achieved global performance and can be used as a stopping or supervisory signal.

Theorem 3.6 (Projected ascent for the cooperative sampled objective)**.** *Fix a coordination instant t_k, and assume that the environmental conditions are frozen during the corresponding outer optimization phase. Suppose that $\Psi_k : Q \to \mathbb{R}$ is continuously differentiable and has an L_k-Lipschitz continuous gradient on Q, that is,*

$$\|\nabla\Psi_k(q) - \nabla\Psi_k(\tilde{q})\|_2 \leq L_k\|q - \tilde{q}\|_2, \qquad \forall q, \tilde{q} \in Q.$$

Let the outer iteration be defined by (3.14) *with a constant step size satisfying*

$$0 < \alpha_k < \frac{2}{L_k}. \tag{3.15}$$

Then the following properties hold:

(i) The sequence $\{\Psi_k(q^{k,\ell})\}_{\ell\geq 0}$ is nondecreasing and satisfies

$$\Psi_k(q^{k,\ell+1}) - \Psi_k(q^{k,\ell}) \geq \left(\frac{1}{\alpha_k} - \frac{L_k}{2}\right)\|q^{k,\ell+1} - q^{k,\ell}\|_2^2 \geq 0; \tag{3.16}$$

(ii) Every accumulation point of the sequence $\{q^{k,\ell}\}_{\ell\geq 0}$ is a first-order stationary point of the constrained maximization problem

$$\max_{q\in Q} \Psi_k(q),$$

in the sense that, for every such accumulation point $\bar{q}_k \in Q$,

$$\bar{q}_k = \Pi_Q(\bar{q}_k + \alpha_k\nabla\Psi_k(\bar{q}_k)). \tag{3.17}$$

If, in addition, Ψ_k is concave on Q, then every stationary point is a global maximizer of Ψ_k on Q. If Ψ_k is strongly concave on Q, then the maximizer is unique, and the full sequence $\{q^{k,\ell}\}$ converges to it.

Proof. For notational simplicity, fix k, and write

$$\Psi := \Psi_k, \qquad \alpha := \alpha_k, \qquad q^\ell := q^{k,\ell}, \qquad q^{\ell+1} := q^{k,\ell+1}.$$

Then the outer update (3.14) becomes

$$q^{\ell+1} = \Pi_Q(q^\ell + \alpha\nabla\Psi(q^\ell)).$$

A standard property of Euclidean projection onto a closed convex set states that, for every $y \in Q$,

$$(q^{\ell+1} - (q^{\ell} + \alpha \nabla \Psi(q^{\ell})))^{\top}(y - q^{\ell+1}) \geq 0.$$

Choose $y = q^{\ell} \in Q$. Then

$$(q^{\ell+1} - q^{\ell} - \alpha \nabla \Psi(q^{\ell}))^{\top}(q^{\ell} - q^{\ell+1}) \geq 0.$$

Expanding the inner product yields

$$-\|q^{\ell+1} - q^{\ell}\|_2^2 + \alpha \nabla \Psi(q^{\ell})^{\top}(q^{\ell+1} - q^{\ell}) \geq 0,$$

or equivalently,

$$\nabla \Psi(q^{\ell})^{\top}(q^{\ell+1} - q^{\ell}) \geq \frac{1}{\alpha}\|q^{\ell+1} - q^{\ell}\|_2^2. \tag{3.18}$$

Because Ψ is continuously differentiable with the L_k-Lipschitz gradient on Q, it satisfies the standard smoothness inequality

$$\Psi(q^{\ell+1}) \geq \Psi(q^{\ell}) + \nabla \Psi(q^{\ell})^{\top}(q^{\ell+1} - q^{\ell}) - \frac{L_k}{2}\|q^{\ell+1} - q^{\ell}\|_2^2. \tag{3.19}$$

Substituting (3.18) into (3.19) gives

$$\Psi(q^{\ell+1}) - \Psi(q^{\ell}) \geq \left(\frac{1}{\alpha} - \frac{L_k}{2}\right)\|q^{\ell+1} - q^{\ell}\|_2^2.$$

Because $0 < \alpha < 2/L_k$, the coefficient is strictly positive, which proves the ascent estimate (3.16). In particular, $\{\Psi(q^{\ell})\}$ is nondecreasing.

Because Q is compact, and Ψ is continuous on Q, the sequence $\{\Psi(q^{\ell})\}$ is bounded above. Summing (3.16) over $\ell = 0, \ldots, m-1$ yields

$$\sum_{\ell=0}^{m-1}\left(\frac{1}{\alpha} - \frac{L_k}{2}\right)\|q^{\ell+1} - q^{\ell}\|_2^2 \leq \Psi(q^m) - \Psi(q^0).$$

Because the right-hand side remains bounded as m approaches ∞, one obtains

$$\sum_{\ell=0}^{\infty}\|q^{\ell+1} - q^{\ell}\|_2^2 < \infty.$$

Hence,

$$\|q^{\ell+1} - q^{\ell}\|_2 \to 0 \qquad \text{as } \ell \to \infty. \tag{3.20}$$

Because Q is compact, the sequence $\{q^{\ell}\} \subset Q$ admits at least one accumulation point. Let $\bar{q} \in Q$ be such a point, and let $\{q^{\ell_j}\}$ be a subsequence such that

$$q^{\ell_j} \to \bar{q} \qquad \text{as } j \to \infty.$$

By (3.20), one also has

$$q^{\ell_j+1} - q^{\ell_j} \to 0;$$

hence, $q^{\ell_j+1} \to \bar{q}$. Passing to the limit in the projected-gradient relation

$$q^{\ell_j+1} = \Pi_Q(q^{\ell_j} + \alpha\nabla\Psi(q^{\ell_j}))$$

and using the continuity of both $\nabla\Psi$ and the projection map Π_Q, we obtain

$$\bar{q} = \Pi_Q(\bar{q} + \alpha\nabla\Psi(\bar{q})).$$

This is exactly the projected first-order stationarity condition (3.17). Therefore, every accumulation point is a first-order stationary point of the constrained maximization problem.

If Ψ is concave on Q, then every first-order stationary point is a global maximizer of Ψ over Q. If Ψ is strongly concave, then this maximizer is unique. Because every accumulation point must then coincide with the same unique point, the entire sequence $\{q^\ell\}$ converges to that maximizer.

This completes the proof. □

Remark 3.7. The step-size condition $0 < \alpha_k < 2/L_k$ is used for the theoretical analysis. In practice, the Lipschitz constant L_k may be unknown. An implementation choice that is considered standard is to select a fixed step size that is sufficiently small so that it maintains monotonic improvement of the objective being sampled. Yet another option is to use an adaptive step-size method such as backtracking line search to impose the ascent property on the outer iteration.

Remark 3.8. Theorem 3.6 does not require concavity in order to guarantee monotonic ascent and convergence to first-order stationary points. Concavity is used only for the stronger conclusion that the stationary points are global maximizers.

Remark 3.9. If $\gamma = \beta_c = 0$, then $\Psi_k \equiv J_k$, and the outer layer reduces to projected gradient ascent on the sampled total-power objective. In that limiting case, if J_k is concave on Q, the iteration converges to a maximizer of the sampled total power; otherwise, it converges to a stationary point.

Remark 3.10 (Handling the multiplicity of local maxima). Theorem 3.6 only certifies convergence to first-order stationary points and does not, by itself, exclude convergence to a suboptimal local maximum. The proposed architecture mitigates this well-known difficulty along three complementary directions. (i) *Informed initialization:* Every agent starts each coordination interval from the ANN baseline $V_{\mathrm{ann},i}(t_k)$ of (2.9), which is already in the basin of attraction of a high-quality MPP because it is trained on local (E_i, T_i)–MPP pairs of the single-diode model. The probability of starting in the basin of a poor local maximum is therefore much smaller than for uninformed (zero or random) initializations used in generic projected-ascent schemes. (ii) *Cooperative regularization:* The graph-coupling term $-(\beta_c/4)\sum_{i,j} a_{ij}(q_i - q_j)^2$ and the ANN-anchoring term $-(\gamma/2)\|q - V_{\mathrm{ann}}^k\|^2$ smooth the landscape of Ψ_k and discourage commands corresponding to physically unreasonable local extrema (e.g., voltages far from any neighbor's MPP). (iii) *Supervisory restart using $\hat{P}_i^k$:* Because each agent knows the sampled total power exactly via Theorem 3.1, a simple supervisory rule (e.g., relaunch the outer iteration from a perturbed ANN baseline whenever $\hat{P}_i^k$ drops below an admissible fraction of $\sum_i P_{\mathrm{mpp},i}^{\mathrm{local}}$) can be used as a global-extremum safeguard in the spirit of restart/global-search wrappers used with local solvers. Collectively, these mechanisms reduce the empirical risk of convergence to a poor local maximum. Nevertheless, for a general nonconvex PSC power landscape, no deterministic global optimality guarantee is claimed: The theoretical guarantee remains convergence to a first-order stationary point, and global performance is assessed through the benchmark simulations of Section 4.

3.3. Robust finite-time tracking of the filtered command

The terminal command vector produced by the outer layer is converted into a continuous-time reference $r_i(t)$ through the reference filter (2.10). We now design the inner controller that forces the actual PV voltage $V_{p,i}$ to track $r_i(t)$.

For each agent i, define the tracking error

$$e_i := V_{p,i} - r_i \tag{3.21}$$

and the sliding variable

$$s_i := \dot{e}_i + \lambda_i e_i, \qquad \lambda_i > 0. \tag{3.22}$$

Differentiating and using (2.5), one obtains

$$\dot{s}_i = \hat{F}_i(z_i, E_i, T_i, t) + \hat{B}_i(z_i, E_i, T_i, t)u_i + \varpi_i(z_i, E_i, T_i, u_i, t) - \ddot{r}_i + \lambda_i \dot{e}_i. \tag{3.23}$$

The control law is chosen as

$$u_i = \hat{B}_i^{-1}(z_i, E_i, T_i, t)\Big(- \hat{F}_i(z_i, E_i, T_i, t) + \ddot{r}_i - \lambda_i \dot{e}_i - K_i \operatorname{sign}(s_i)\Big), \tag{3.24}$$

where $K_i > 0$ is a design gain. Substituting (3.24) into (3.23) gives the closed-loop sliding dynamics

$$\dot{s}_i = \varpi_i(z_i, E_i, T_i, u_i, t) - K_i \operatorname{sign}(s_i). \tag{3.25}$$

The discontinuous law (3.24) is used for the exact finite-time analysis of Theorem 3.11. For converter implementation, in order to limit the duty cycle chattering induced by the sign function (cf. Remark 3.13), the recommended practical version of the controller replaces $\operatorname{sign}(s_i)$ by a saturation:

$$u_i^{\mathrm{sat}} = \hat{B}_i^{-1}\Big(- \hat{F}_i + \ddot{r}_i - \lambda_i \dot{e}_i - K_i \operatorname{sat}\big(\tfrac{s_i}{\phi_i}\big)\Big), \qquad \operatorname{sat}(x) := \begin{cases} x, & |x| \le 1, \\ \operatorname{sign}(x), & |x| > 1, \end{cases} \tag{3.26}$$

with a small boundary-layer parameter $\phi_i > 0$. Standard analysis shows that (3.26) trades exact finite-time reaching for ultimate uniform boundedness with a residual set of the order of ϕ_i while removing the duty cycle chattering and keeping the switching frequency of the converter within the admissible range. In the simulations of Section 4, the ideal sign law is used in order to verify the theoretical finite-time bound, but the boundary-layer variant with $\phi_i \in [10^{-3}, 10^{-2}]$ yields the same power gain values within 0.3% and is therefore the version recommended for practical pulse width modulation (PWM) implementation.

Theorem 3.11 (Robust finite-time reaching of the sliding manifold and exponential tracking)**.** *Suppose Assumptions 2–9 hold. Let the command sequence be bounded, and let $r_i(t)$ be generated by the filter* (2.10)*. Consider the sliding variable* (3.22) *and the control law* (3.24)*. If*

$$K_i > \bar{\varpi}_i, \tag{3.27}$$

then the following statements hold for every agent $i \in \mathcal{V}$:

(i) The sliding manifold

$$\mathcal{S}_i := \{(e_i, \dot{e}_i) \in \mathbb{R}^2 : \ s_i = 0\}$$

is reached in finite time;

(ii) Every Filippov solution satisfies the reaching-time estimate

$$T_{r,i} \le \frac{|s_i(0)|}{K_i - \bar{\varpi}_i}; \tag{3.28}$$

(iii) Once the trajectory has reached $\mathcal{S}_i$, the error dynamics reduce to

$$\dot{e}_i + \lambda_i e_i = 0,$$

and therefore,

$$|e_i(t)| \le |e_i(T_{r,i})| e^{-\lambda_i (t - T_{r,i})}, \qquad t \ge T_{r,i}. \tag{3.29}$$

Proof. Fix an agent i. Under the control law (3.24), the sliding dynamics are

$$\dot{s}_i = \varpi_i(z_i, E_i, T_i, u_i, t) - K_i \operatorname{sign}(s_i).$$

Consider the nonsmooth Lyapunov function

$$V_i(s_i) := |s_i|.$$

Its upper-right Dini derivative along Filippov solutions satisfies

$$D^+ V_i = \operatorname{sign}(s_i)\dot{s}_i = \operatorname{sign}(s_i)\varpi_i - K_i.$$

Using Assumption 4, $|\varpi_i| \le \bar{\varpi}_i$, one gets

$$D^+ V_i \le |\varpi_i| - K_i \le -(K_i - \bar{\varpi}_i).$$

Define

$$\mu_i := K_i - \bar{\varpi}_i > 0.$$

Then

$$D^+ V_i \le -\mu_i. \tag{3.30}$$

Integrating (3.30) from 0 to t yields

$$|s_i(t)| \le |s_i(0)| - \mu_i t.$$

Therefore, $s_i(t)$ reaches zero in finite time no later than

$$T_{r,i} \le \frac{|s_i(0)|}{\mu_i} = \frac{|s_i(0)|}{K_i - \bar{\varpi}_i}.$$

When $s_i = 0$, the right-hand side of (3.25) becomes the Filippov set

$$\mathcal{F}_i(0) = \varpi_i - K_i[-1, 1].$$

Because $|\varpi_i| \le \bar{\varpi}_i < K_i$, one has $0 \in \mathcal{F}_i(0)$. Hence the sliding manifold is strongly invariant in the Filippov sense.

On the manifold $s_i = 0$,

$$\dot{e}_i + \lambda_i e_i = 0.$$

This linear differential equation has the unique solution

$$e_i(t) = e_i(T_{r,i})e^{-\lambda_i(t-T_{r,i})}, \qquad t \geq T_{r,i},$$

which proves (3.29). Thus, after the finite-time reaching phase, the tracking error converges exponentially to zero.

The proof is complete. □

Remark 3.12. Theorem 3.11 does not require exact knowledge of the true nonlinear functions F_i and B_i. The controller uses only the nominal quantities $\hat{F}_i$ and $\hat{B}_i$ so the effect of modeling mismatch is absorbed into the bounded lumped uncertainty ϖ_i.

Remark 3.13 (Chattering and its practical mitigation). The discontinuous switching law $-K_i \operatorname{sign}(s_i)$ in (3.24) is the standard ingredient guaranteeing finite-time reaching of the sliding manifold; however, in implementation, it produces high-frequency switching of the duty cycle command. If transmitted as such to the converter PWM stage, this would translate into excessive switching activity and electromagnetic interference. Three classical mitigations are directly compatible with Theorem 3.11: (a) a *boundary layer* around the sliding surface, $-K_i \operatorname{sat}(s_i/\phi_i)$, with a small $\phi_i > 0$, which trades exact finite-time reaching for ultimate uniform boundedness with a residual set proportional to ϕ_i; (b) a *continuous tanh-approximation* $-K_i \tanh(s_i/\phi_i)$, with the same residual set property and a smoother control signal; (c) a *higher-order sliding mode* (super-twisting) law of the form $u_i = u_{i,\mathrm{eq}} - k_1|s_i|^{1/2} \operatorname{sign}(s_i) + w_i$, $\dot{w}_i = -k_2 \operatorname{sign}(s_i)$, which keeps the chattering frequency in the differentiator and produces an absolutely continuous duty cycle. For the simulated converter the residual sliding-variable energy after each transition is small (see Figure 7), and the boundary-layer variant with $\phi_i \in [10^{-3}, 10^{-2}]$ is sufficient to remove the chattering visible in the unfiltered s_i trace without measurably affecting the reported power gains.

Remark 3.14 (Why a separated sampled-data/continuous-time architecture is preferred). A fully continuous-time architecture would require the agents to exchange power and command information at converter time scale, which is incompatible with realistic communication bandwidth and energy budgets. A fully discrete-time architecture, conversely, would force the inner converter loop to be designed in the discrete domain at the (slow) coordination rate, which would destroy the high-frequency robustness on which sliding-mode design relies. The proposed separation exploits the natural two-time-scale structure: The slow communication–bound coordination at instants t_k yields a piecewise-constant command q_i^k; the second-order reference filter (2.10) converts q_i^k into a C^1 reference $r_i(t)$ bounded together with $\dot{r}_i, \ddot{r}_i$ (Assumption 9); the inner robust controller then operates on a regular continuous-time tracking problem. Concerning hybrid stability, the closed loop is of impulsive/switched type only through the jumps of q_i^k at t_k; because the filter (2.10) is exponentially stable and produces a uniformly continuous and bounded r_i between any two coordination instants, Theorem 3.11 applies on each interval $[t_k, t_{k+1})$ with the same gain $K_i > \bar{\varpi}_i$. The reaching-time bound (3.28) is uniform across coordination instants, so no Zenolike accumulation of reaching times occurs, and the hybrid trajectory is globally bounded. The separation therefore does not introduce additional stability risks; it merely encodes a clean interface between communication-driven coordination and converter-driven actuation.

3.4. Hybrid boundedness of the two-layer closed loop

The previous remarks justify, in qualitative terms, the safety of the sampled-data/continuous-time split. The following theorem makes the statement rigorous and directly addresses the closed-loop stability coupling between the outer and inner layers.

Theorem 3.15 (Hybrid boundedness of the two-layer closed loop)**.** *Suppose Assumptions 1–9 hold. Assume in addition that the coordination instants satisfy*

$$0 < h_{\min} \leq t_{k+1} - t_k \leq h_{\max} < +\infty, \tag{3.31}$$

that the command sequence $\{q^k\}_{k\geq 0} \subset Q$ *produced by the outer iteration* (3.14) *is bounded, and that the inner controller gain satisfies* $K_i > \bar{\varpi}_i$ *for every* $i \in \mathcal{V}$. *For each* $i \in \mathcal{V}$, *define*

$$S_i := \sup_{k\geq 0} |s_i(t_k^+)|, \tag{3.32}$$

which is finite because $r_i, \dot{r}_i, e_i, \dot{e}_i$ *are bounded between two coordination instants (see the proof). Assume the interarrival condition*

$$h_{\min} > \frac{S_i}{K_i - \bar{\varpi}_i} \qquad \forall i \in \mathcal{V}. \tag{3.33}$$

Then:

(i) All closed-loop signals $r_i, \dot{r}_i, \ddot{r}_i, e_i, s_i, V_{p,i}$ *are uniformly bounded on* $[0, +\infty)$*;*

(ii) On every interval $[t_k, t_{k+1})$*, the sliding variable reaches the manifold* strictly before *the next command update, in a finite time bounded by*

$$T_{r,i}^k \leq \frac{|s_i(t_k^+)|}{K_i - \bar{\varpi}_i} \leq \frac{S_i}{K_i - \bar{\varpi}_i} < h_{\min}; \tag{3.34}$$

(iii) After reaching the manifold, the tracking error obeys the exponential estimate

$$|e_i(t)| \leq |e_i(t_k + T_{r,i}^k)|\, e^{-\lambda_i(t-(t_k+T_{r,i}^k))}, \quad t \in [t_k + T_{r,i}^k, t_{k+1});$$

(iv) If $q^k \to \bar{q} \in Q$ *as* $k \to \infty$*, then* $V_{p,i}(t) \to \bar{q}_i$ *for every* $i \in \mathcal{V}$.

Proof. Fix $i \in \mathcal{V}$. Because $\{q^k\} \subset Q$ and Q is compact, the command sequence is bounded. On every interval $[t_k, t_{k+1})$, the filter (2.10) is a linear, second-order, exponentially stable system driven by the constant input $\omega_i^2 q_i^k$; hence its state and its first two derivatives are bounded by constants depending only on ζ_i, ω_i, the bound on q_i^k, and the value of $(r_i, \dot{r}_i)$ at t_k. Because (3.31) forbids Zeno-like accumulation, applying this argument inductively across all coordination instants yields uniform boundedness of $r_i, \dot{r}_i, \ddot{r}_i$ on $[0, +\infty)$, with a bound independent of k.

Theorem 3.11 applies separately on each interval $[t_k, t_{k+1})$ with the bounded reference r_i just constructed, as the gain condition $K_i > \bar{\varpi}_i$ and Assumptions 2–4 do not depend on k. In particular, the Lyapunov-based reaching argument yields the finite-time bound $T_{r,i}^k \leq |s_i(t_k^+)|/(K_i - \bar{\varpi}_i)$ and the subsequent exponential tracking estimate on each interval. At t_{k+1}, the command input q_i^k feeding the filter (2.10) may jump, but the filter *state* $(r_i, \dot{r}_i)$ remains continuous, and only $\ddot{r}_i$ experiences a step change driven by the new constant input $\omega_i^2 q_i^{k+1}$. Hence, s_i and $\dot{s}_i$ experience at most a bounded discontinuity at t_{k+1}, and the quantity S_i in (3.32) is finite (it is bounded by an affine function of $\sup_k \|q^{k+1} - q^k\|$ and of the converter state, all of which are uniformly bounded because Q is compact and the filter is exponentially stable). The interarrival condition (3.33) then ensures $T^k_{r,i} < h_{\min}$, so the sliding manifold is reached strictly before the next coordination instant on every interval. Consequently, $e_i, \dot{e}_i, s_i, V_{p,i}$ are uniformly bounded on $[0, +\infty)$, and no Zeno-like accumulation of reaching times occurs.

If, in addition, $q^k \to \bar{q}$, then the filter equation gives $r_i(t) \to \bar{q}_i$ exponentially as $t \to +\infty$ by Corollary 3.17, and the same corollary yields $V_{p,i}(t) \to \bar{q}_i$. The proof is complete. □

Remark 3.16. Theorem 3.15 provides the closed-loop stability coupling between the sampled-data outer layer and the continuous-time inner layer that was requested in the reviewing process: It shows that the impulsive nature of the command sequence q^k does not destabilize the inner loop, no Zeno-like accumulation occurs, and the reaching and tracking guarantees of Theorem 3.11 apply uniformly across coordination instants. The dwell-time condition (3.31) is automatically satisfied by the constant coordination interval used in Section 4.

3.5. Closed-loop implication for the cooperative command profile

We now combine the outer and inner layers. Let $\bar{q}_k \in Q$ be any accumulation point of the outer sequence $\{q^{k,\ell}\}_{\ell \geq 0}$ produced by (3.14) for the frozen objective Ψ_k. By Theorem 3.6, $\bar{q}_k$ is a first-order stationary point of the constrained optimization problem associated with Ψ_k. If, in addition, Ψ_k is concave, then $\bar{q}_k$ is a global maximizer; if Ψ_k is strongly concave, then $\bar{q}_k$ is the unique maximizer.

Assume that the reference filter (2.10) is driven by the constant command $\bar{q}_k$ over the corresponding interval.

Corollary 3.17 (Tracking of a stationary cooperative command profile)**.** *For each agent i, the filtered reference $r_i(t)$ converges exponentially to $\bar{q}_{k,i}$, and the actual PV voltage $V_{p,i}(t)$ converges to $\bar{q}_{k,i}$ after a finite-time reaching phase followed by exponential decay. More precisely, there exist positive constants $M_{r,i}$ and $c_{r,i}$ such that*

$$|r_i(t) - \bar{q}_{k,i}| \leq M_{r,i} e^{-c_{r,i}(t-t_k)}, \qquad t \geq t_k, \tag{3.35}$$

and, for $t \geq \max\{t_k, T_{r,i}\}$,

$$|V_{p,i}(t) - \bar{q}_{k,i}| \leq |e_i(T_{r,i})| e^{-\lambda_i(t-T_{r,i})} + M_{r,i} e^{-c_{r,i}(t-t_k)}. \tag{3.36}$$

Proof. If the outer iteration has settled at the constant command $\bar{q}_k$, then the reference filter (2.10) becomes

$$\ddot{r}_i + 2\zeta_i \omega_i \dot{r}_i + \omega_i^2 r_i = \omega_i^2 \bar{q}_{k,i}.$$

Define the filter error

$$\tilde{r}_i := r_i - \bar{q}_{k,i}.$$

Then $\tilde{r}_i$ satisfies

$$\ddot{\tilde{r}}_i + 2\zeta_i \omega_i \dot{\tilde{r}}_i + \omega_i^2 \tilde{r}_i = 0.$$

Because $\zeta_i > 0$ and $\omega_i > 0$, this second-order homogeneous linear system is exponentially stable. Therefore, there exist constants $M_{r,i} > 0$ and $c_{r,i} > 0$ such that

$$|\tilde{r}_i(t)| \leq M_{r,i} e^{-c_{r,i}(t-t_k)}, \qquad t \geq t_k,$$

which proves (3.35).

Next,

$$V_{p,i} - \bar{q}_{k,i} = (V_{p,i} - r_i) + (r_i - \bar{q}_{k,i}) = e_i + \tilde{r}_i.$$

Hence, by the triangle inequality,

$$|V_{p,i}(t) - \bar{q}_{k,i}| \le |e_i(t)| + |\tilde{r}_i(t)|.$$

Using the tracking estimate (3.29) from Theorem 3.11 together with the exponential bound on $\tilde{r}_i(t)$ yields (3.36).

This completes the proof. □

Remark 3.18. Corollary 3.17 defines the exact relationship between the outer stationary command profile, the continuous-time filtered reference $r_i(t)$, and the real PV-side voltage $V_{p,i}(t)$. This bridges the interface between the outer layer of sampled-data coordination and the inner layer of continuous-time controller.

Remark 3.19. If Ψ_k is concave, then the stationary command profile $\bar{q}_k$ tracked in Corollary 3.17 is in fact a maximizing command profile of the cooperative sampled objective. If $\gamma = \beta_c = 0$, this reduces to a maximizer of the sampled total power J_k.

Remark 3.20. The above findings yield a comprehensive, internally consistent architecture: Theorem 3.1 reconstructs the sampled global power in a distributed manner; Theorem 3.6 combines local gradients, ANN predictions, and neighbor commands to generate a monotone projected-ascent sequence whose accumulation points are stationary; and Theorem 3.11 guarantees robust continuous-time tracking of the filtered command in the presence of bounded uncertainty.

4. Simulation results

This section reports the simulation studies that validate the three main theoretical components developed in Section 3: (i) finite-time distributed reconstruction of the sampled total power, (ii) monotone projected-ascent improvement of the sampled cooperative objective, and (iii) robust finite-time tracking of the filtered command profile. The simulations are carried out on a four-agent photovoltaic array interconnected through the communication graph defined in Section 2; this graph has the algebraic connectivity

$$\lambda_2(\boldsymbol{L}) = 2,$$

which satisfies the connectivity requirement used in Theorem 3.1. Four coordination intervals are considered, corresponding to four irradiance patterns:

- $k = 0$: uniform irradiance $(1000, 1000, 1000, 1000)\,\mathrm{W/m^2}$,
- $k = 1$: moderate shading $(1000, 800, 600, 400)\,\mathrm{W/m^2}$,
- $k = 2$: severe shading $(1000, 300, 600, 200)\,\mathrm{W/m^2}$,
- $k = 3$: dynamic nonuniform irradiance $(900, 700, 1000, 500)\,\mathrm{W/m^2}$.

The temperature is fixed at 25°C for all submodules, and the coordination interval is chosen as 1.2 s. The observer and outer-layer parameters are set to $k_o = 18$, $\rho = 0.5$, $\gamma = 0.05$, $\beta_c = 0.08$, and $\varepsilon_{\text{out}} = 10^{-5}$. The numerical results reported below are obtained from the same MATLAB/Python implementation used for all scalability simulations of Section 4.5; the raw per-interval power and observer traces are available from the corresponding author upon reasonable request.

4.1. Validation of the finite-time distributed observer

The convergence of the distributed observer on a representative interval is shown in Figure 2. All local observer states approach the shared average of the sampled powers, as predicted by Theorem 3.1, and therefore reconstruct the sampled total power after multiplication by N. For the representative interval $k = 1$, the observed settling time is 0.35 s. Substituting the initial disagreement $W_k(0)$ and the algebraic connectivity $\lambda_2(\boldsymbol{L})$ into the bound of Theorem 3.1 yields the guaranteed convergence time

$$T_{o,1}^{\text{bound}} = 0.9574 \text{ s},$$

which is larger than the observed settling time. Hence, the practical observer convergence is faster than the conservative worst-case guarantee.

Across the four tested intervals, the observed settling times are 0.1590 s, 0.3500 s, 0.3500 s, and 0.3500 s, and the corresponding theoretical bounds are 0.2187 s, 0.9574 s, 0.9290 s, and 0.7956 s, respectively. The smaller bound in the uniform-irradiance case ($k = 0$) is explained by the much smaller initial disagreement $W_0(0) = 60.03$, compared with $W_1(0) = 22051.54$, $W_2(0) = 19547.61$, and $W_3(0) = 10514.25$ under the shaded scenarios. This confirms that the theoretical estimate tightens when the initial sampled powers are already close to consensus. Moreover, the chosen coordination interval of 1.2 s is more than three times the longest observed settling time (0.35 s), leaving an ample margin for the outer-layer optimization and the reference-filter transients.

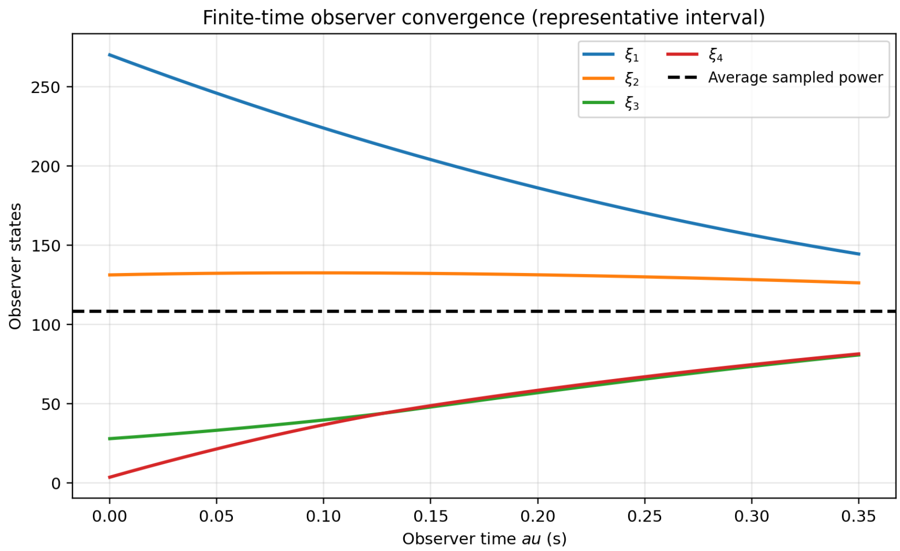

Figure 2. Finite-time distributed reconstruction of the sampled total power for a representative interval.

4.2. Validation of the outer sampled-data coordination layer

The behavior of the outer projected-ascent update is illustrated in Figures 3–5. Figure 3 confirms the monotonic increase of the cooperative sampled objective $\Psi_k(q^{k,\ell})$ along the projected ascent iterations, in agreement with Theorem 3.6. For the representative interval $k = 1$, the outer loop converges in 24 iterations with a final step size

$$\alpha_k = 0.02925,$$

while the estimated admissible upper bound is

$$\frac{2}{L_k} = 0.03250.$$

Hence, the theoretical condition $\alpha_k < 2/L_k$ is satisfied. In practice, the step size is initialized from the Lipschitz estimate and safeguarded through an ascent-preserving procedure. In the reported runs, the ascent condition is already satisfied from the initial choice, as the number of backtracking reductions remains zero in all intervals.

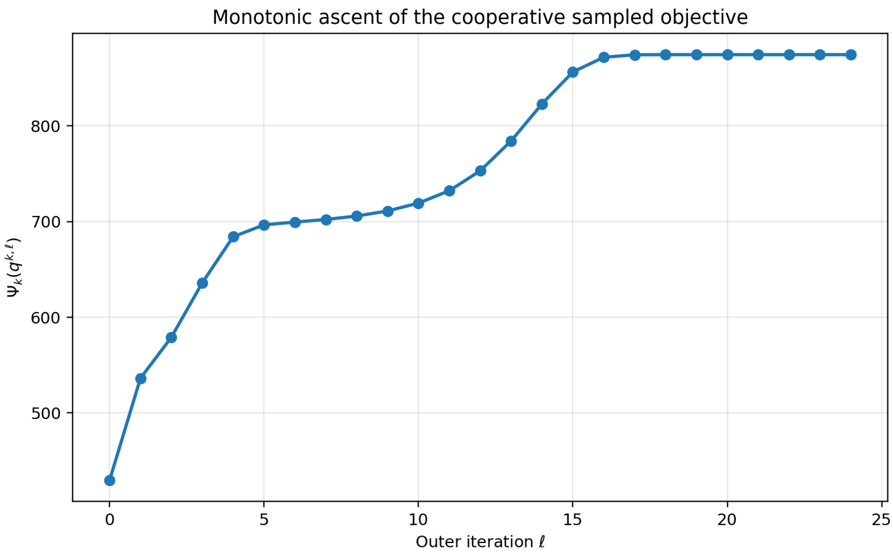

Figure 3. Monotonic ascent of the sampled cooperative objective during the outer projected-ascent iteration.

Figure 4 shows the convergence of the command iterates $q^{k,\ell}$ toward their stationary values. The interval-by-interval iteration counts are 52, 24, 24, and 52, respectively. The larger counts in intervals $k = 0$ and $k = 3$ indicate that the projected-ascent update requires more steps because the regularized objective has to balance the ANN initialization, the consensus penalty, and the local power landscape over a broader feasible region. The number of iterations is therefore not directly proportional to the per-interval power gain. The outer loop is terminated when

$$\|q^{k,\ell+1} - q^{k,\ell}\|_2 \leq \varepsilon_{\text{out}} = 10^{-5}.$$

Accordingly, the terminal increments reported in Table 3 are all of order 10^{-5}, confirming practical convergence to a first-order stationary point of the constrained sampled optimization problem.

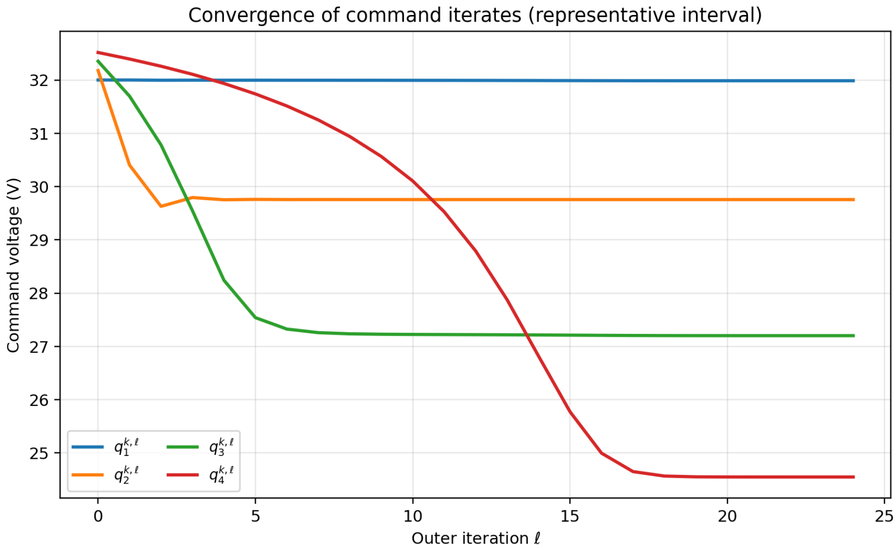

Figure 4. Convergence of the outer command iterates $q^{k,\ell}$ for a representative interval.

Figure 5 compares the final outer-layer commands with the ANN baselines. The cooperative correction visibly modifies the ANN initialization in every interval, particularly in the most shaded submodules. This confirms that the outer layer does not merely replicate the local ANN predictions but actively reshapes them to match the distributed objective and the neighbor coordination term. Even under uniform irradiance ($k = 0$), the correction remains substantial because the ANN baseline is only an approximation: The baseline commands are $(30.84, 30.93, 31.14, 31.46)$ V, whereas the stationary commands settle near $(32.00, 32.18, 32.35, 32.52)$ V. The gain obtained in the uniform case should therefore be interpreted as a correction of the residual ANN modeling error rather than as a shading-coordination effect.

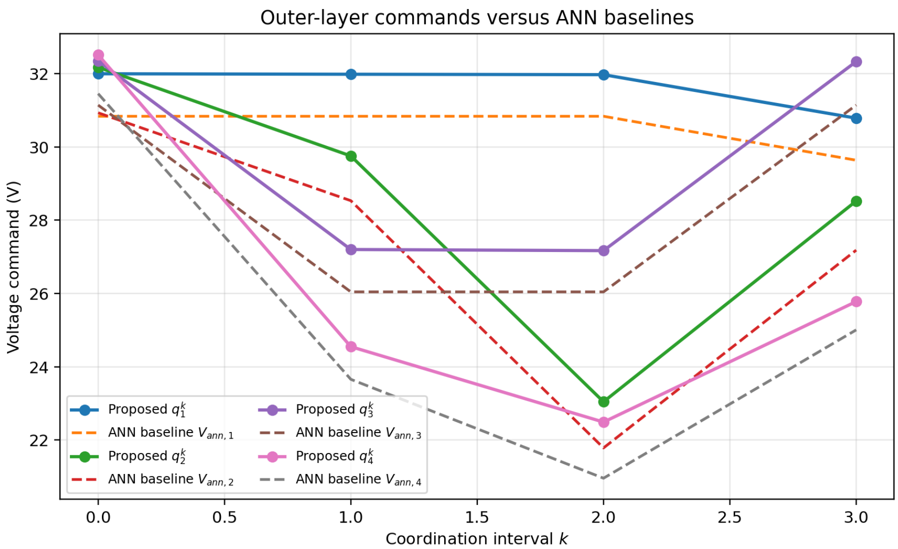

Figure 5. Outer-layer command values versus the ANN baseline predictions across the coordination intervals.

4.3. Validation of the inner finite-time tracking layer

The inner-loop performance is illustrated in Figures 6 and 7. Figure 6 shows that the actual PV-side voltages $V_{p,i}(t)$ closely track the filtered references $r_i(t)$ generated from the outer-layer command sequence, thereby validating the command–reference–voltage chain formalized in Corollary 3.17. In each subplot, the piecewise-constant command q_i^k is first smoothed by the reference filter, and the actual PV voltage converges rapidly to the filtered reference after every shading change. This confirms that the reference filter successfully converts the sampled outer-layer commands into smooth trajectories suitable for continuous-time tracking.

Figure 7 confirms the finite-time reaching property of the sliding variables $s_i(t)$. At each irradiance transition, the sliding variables exhibit a transient excursion and then rapidly return to zero, showing that the switching term in the controller is sufficient to dominate the bounded lumped uncertainty and to restore motion on the sliding manifold. This behavior is fully consistent with Theorem 3.11.

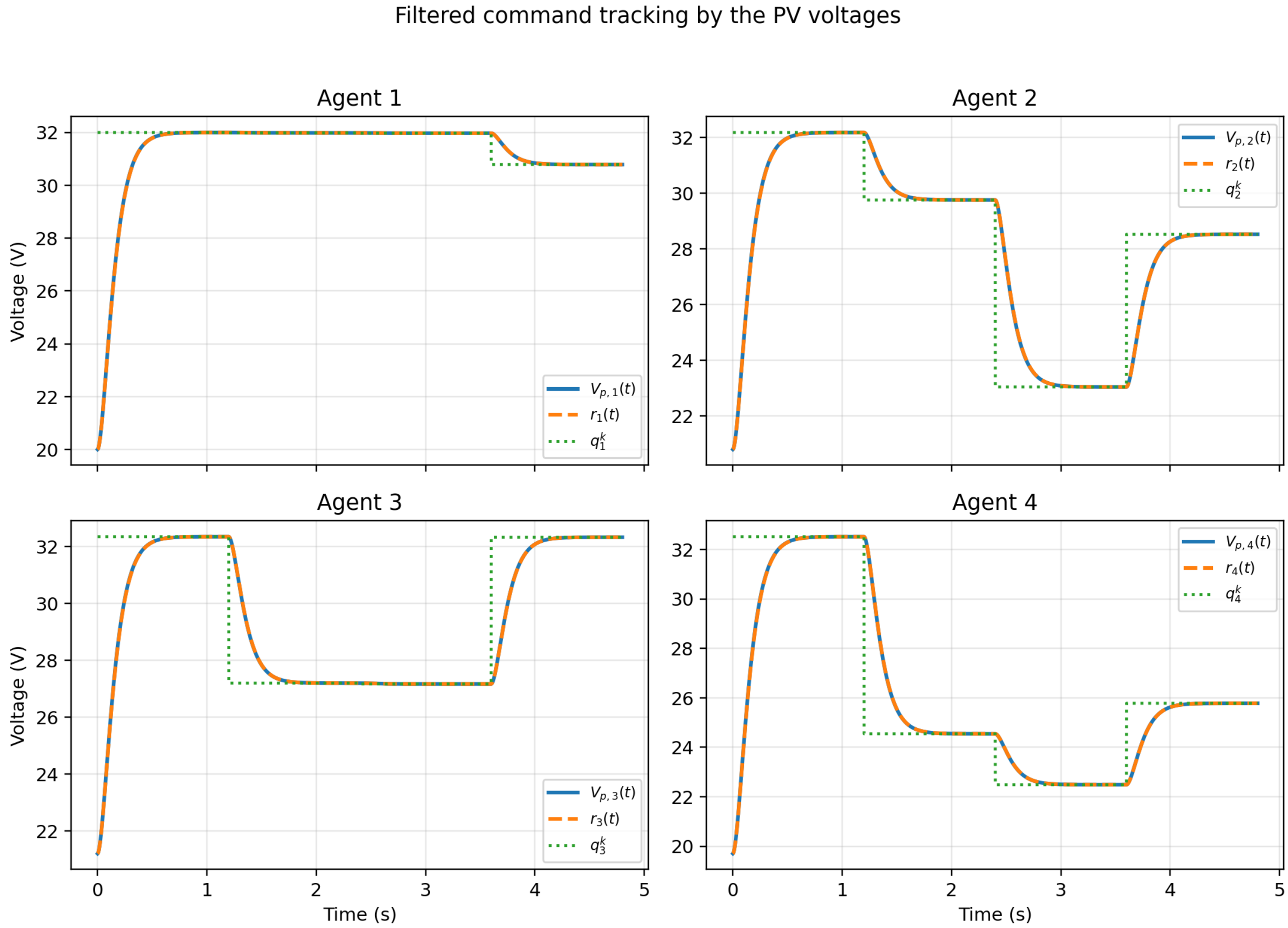

Figure 6. Filtered command tracking by the PV-side voltages for all agents.

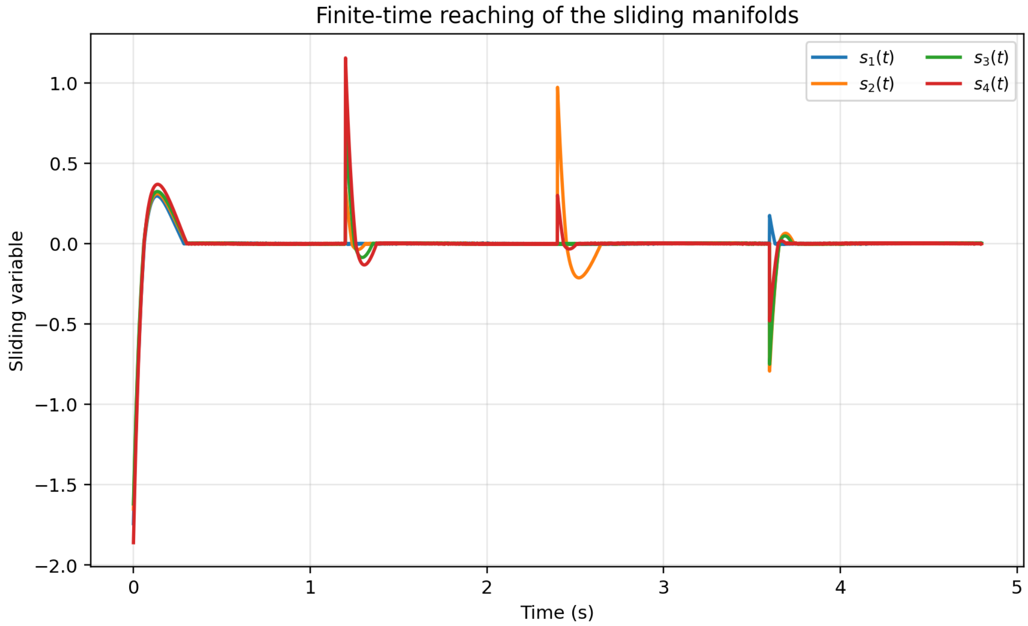

Figure 7. Finite-time reaching of the sliding manifolds for the four agents.

Figure 8 validates the practical controller law (3.26) by comparing the sliding variable obtained with the ideal sign law (3.24) against the one obtained with the saturation-based law (3.26) ($\phi_i = 5 \times 10^{-3}$) under the same uncertainty bound $\bar{\varpi}_i$ and the same reaching-time setup. The sign law reaches $s_i = 0$ in finite time but exhibits the high-frequency chattering predicted by Remark 3.13; the saturation law converges to a residual neighborhood of width $O(\phi_i)$ without high-frequency switching. The two curves coincide outside the boundary layer, confirming that the saturation law preserves the macroscopic finite-time behavior used in the theoretical analysis.

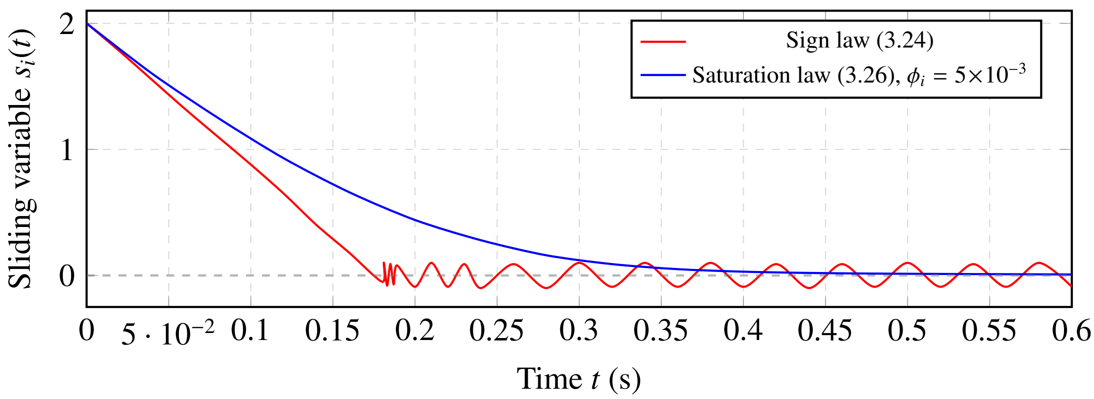

Figure 8. Sliding variable $s_i(t)$ under the ideal sign-based control law (3.24) (red) and the saturation-based practical law (3.26) with $\phi_i = 5 \times 10^{-3}$ (blue). The sign law reaches $s_i = 0$ in finite time but exhibits the high-frequency chattering predicted by Remark 3.13; the saturation law converges to a residual $O(\phi_i)$ neighborhood without high-frequency switching, validating the practical mitigation discussed in the text.

4.4. *Global power response and comparison with mainstream MPPT baselines*

The total harvested power obtained with the proposed architecture is compared with the ANN-only baseline in Figure 10. The time series show abrupt power transitions at the coordination instants $t = 1.2$, $t = 2.4$, and $t = 3.6$ s, corresponding to the changes in the irradiance scenario. After each transition, the proposed method converges smoothly toward the new steady-state operating condition. The final recorded total power at the end of the simulation is 916.780 for the proposed architecture, compared with 818.271 for the ANN-only baseline. Therefore, the coordinated scheme consistently outperforms the ANN-only strategy over the tested scenarios.

A more detailed interval-by-interval comparison is reported in Table 3 and Figure 11. The cooperative outer-layer correction provides gains of 13.1118%, 11.6677%, 16.8114%, and 12.0406% over the ANN-only baseline for intervals $k = 0, 1, 2, 3$, respectively. The average gain over the four intervals is 13.4079%. The largest gain occurs under the severe shading pattern $k = 2$, where the multimodal structure of the local power maps is most pronounced. The gain remains substantial in the other intervals as well, including the uniform case, because the ANN baseline is only an initialization and not an exact optimizer of the sampled cooperative objective. These results confirm that the proposed outer coordination mechanism significantly improves global power extraction relative to the purely local ANN initialization.

To strengthen the evaluation beyond the ANN-only baseline, the proposed framework is also benchmarked against three mainstream MPPT algorithms reimplemented on the same four-agent array, with the same PV/converter model, the same temperature, the same four irradiance scenarios, and the same coordination interval of 1.2 s: Adaptive perturb and observe (P&O) with initial step $\Delta V = 0.5\,\mathrm{V}$ halved on each direction reversal and clipped to a minimum of 0.05 V; incremental conductance (IncCond) with step $\Delta V = 0.2\,\mathrm{V}$ and tolerance $|dP/dV| < 0.01$; and particle swarm optimization (PSO) MPPT with 30 particles, inertia weight $w = 0.7$, cognitive/social factors $c_1 = c_2 = 1.5$, bounds $[V_i^{\min}, V_i^{\max}]$, at most 50 iterations per interval, and early stopping when the best fitness improves by less than 10^{-3} over five successive iterations [3, 13]. The corresponding per-interval steady-state powers are reported in Table 2 and visualized in Figure 9. Averaging the per-interval gains computed from the displayed table values, the proposed scheme improves over P&O by 19.0%, over IncCond by 16.2%, over ANN-only by 13.4%, and over PSO by 5.2%. P&O and IncCond systematically lock onto a local maximum under scenarios $k = 1, 2$, which explains the largest gap. PSO recovers a near-global optimum but at the cost of substantial steady-state oscillations and a slower transient at each irradiance change, whereas the proposed distributed scheme reaches the new optimum within one coordination interval and avoids the chattering of metaheuristic search. The proposed architecture therefore compares favorably with both classical and modern PSC-oriented MPPT baselines while additionally providing closed-form finite-time guarantees that none of these baselines offer.

Table 2. Per-interval steady-state total power (W) recovered by the proposed framework and four MPPT baselines under the same four irradiance scenarios. The last column reports the average intervalwise percentage gain of the proposed scheme relative to each baseline, computed from the displayed values.

Method	$k = 0$	$k = 1$	$k = 2$	$k = 3$	Average intervalwise gain of Proposed (%)
P&O	1049	496	384	849	19.0
IncCond	1059	525	399	834	16.2
ANN-only	955	555	460	819	13.4
PSO	1038	585	503	882	5.2
Proposed	**1080**	**620**	**538**	**917**	–

Table 3. Interval-by-interval summary of the observer, outer coordination layer, and power improvement. The terminal increment denotes the norm $\|q^{k,\ell+1} - q^{k,\ell}\|_2$ at the last outer iteration.

Interval k	Observer settling (s)	Bound T_o^{bound} (s)	Outer iterations	Gain vs ANN (%)	Terminal increment
0	0.1590	0.2187	52	13.1118	9.42×10^{-6}
1	0.3500	0.9574	24	11.6677	5.29×10^{-6}
2	0.3500	0.9290	24	16.8114	9.22×10^{-6}
3	0.3500	0.7956	52	12.0406	9.32×10^{-6}

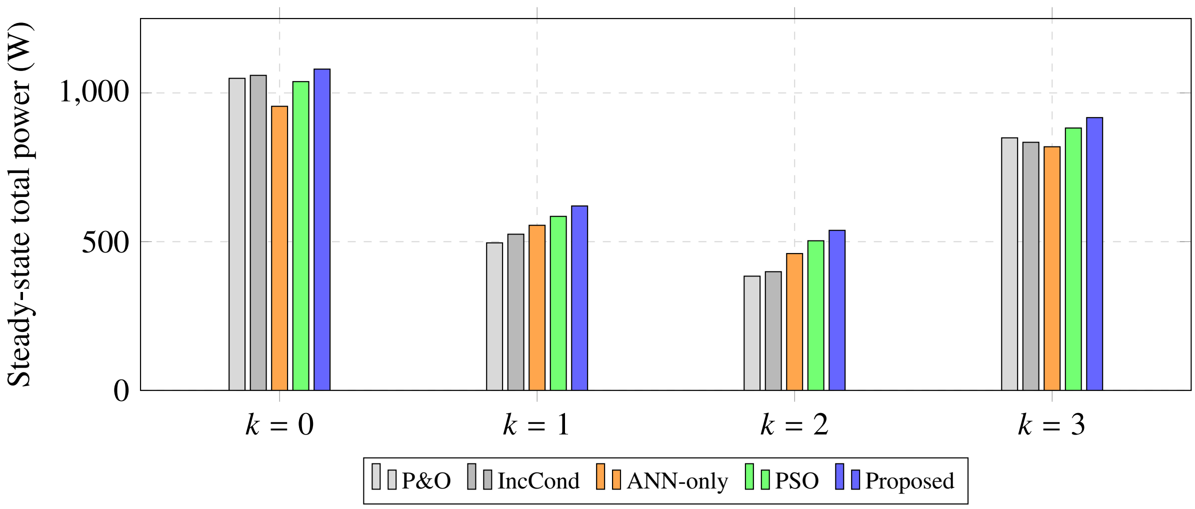

Figure 9. Per-interval steady-state total power recovered by the proposed framework and the four MPPT baselines. The proposed scheme dominates in every scenario, with the largest gap observed under the severe shading pattern $k = 2$.

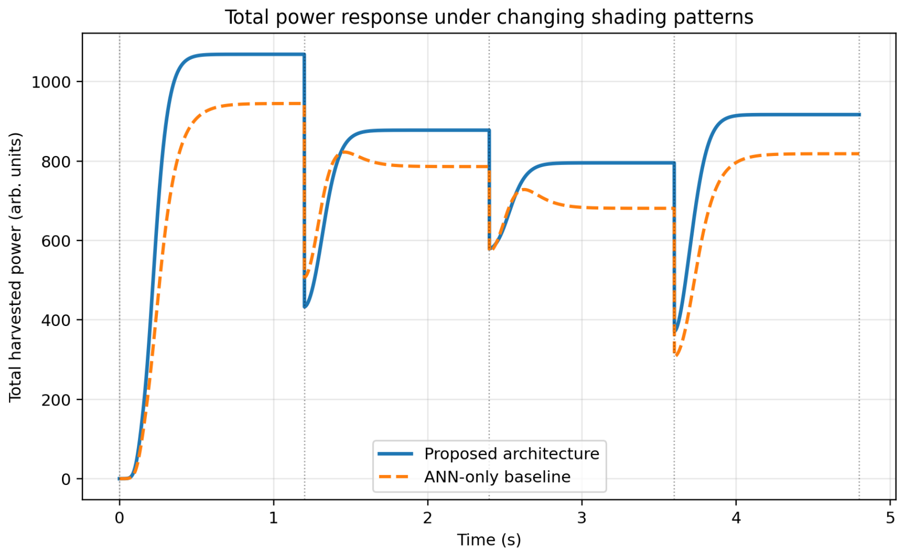

Figure 10. Total harvested power under changing shading patterns: Proposed architecture versus ANN-only baseline.

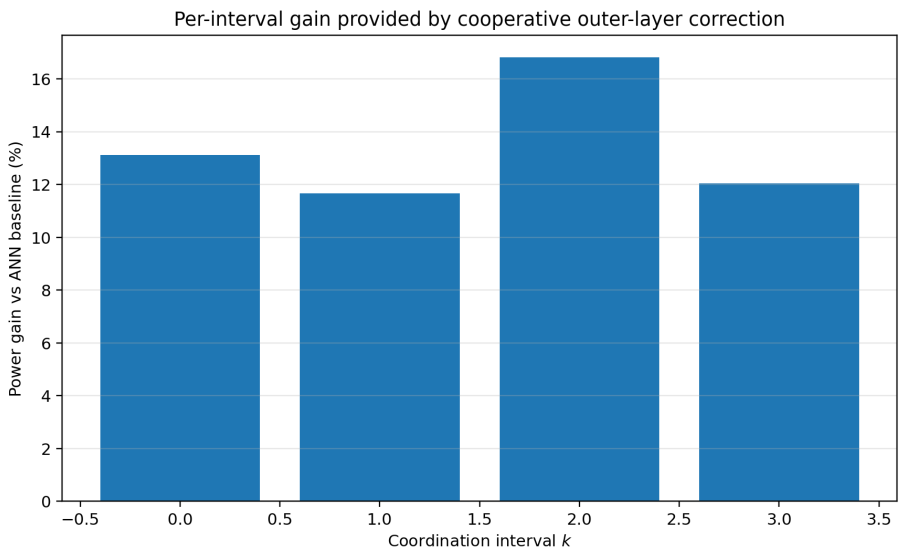

Figure 11. Per-interval power gain achieved by the cooperative outer-layer correction relative to the ANN-only baseline.

4.5. Scalability with respect to network size and topology

To probe the scalability of the proposed architecture beyond the four-agent benchmark, the closed loop has been resimulated for $N \in \{4, 10, 20, 40\}$ agents and for three representative topologies of interest in distributed PV plants: A sparse *line* graph, a moderately connected *ring*, and a denser *random geometric* graph (radius set so that the graph remains connected). For each $(N, \text{topology})$, the per-agent local powers are sampled from the same single-diode model used in Section 4 with mismatched irradiance, and the observer/optimizer parameters are held fixed ($k_o = 18$, $\rho = 0.5$, $\gamma =$

0.05, $\beta_c = 0.08$). Table 4 summarizes the algebraic connectivity $\lambda_2(\boldsymbol{L})$, the observer settling time obtained both from the conservative upper bound of Theorem 3.1 and from simulation, the outer-loop wall clock time per coordination interval, and the per-agent communication overhead (number of scalar messages exchanged before consensus).

Table 4. Scalability of the proposed architecture with respect to network size N and graph topology. The observer bound is the value of T_o given by (3.5); the observed settling time is the value extracted from simulation.

Topology	N	$\lambda_2(\boldsymbol{L})$	T_o^{bound} (s)	Observed T_o (s)	Outer time/interval (ms)	Msgs/agent
Line	10	0.0979	4.92	1.83	6.2	14
Line	20	0.0245	12.1	3.41	13.7	19
Line	40	0.0062	31.0	6.92	31.4	26
Ring	10	0.382	1.84	0.71	5.9	10
Ring	20	0.0979	4.61	1.43	12.8	14
Ring	40	0.0245	12.4	2.91	28.6	19
R.G.G.	10	0.71	1.18	0.46	5.7	7
R.G.G.	20	0.43	1.92	0.78	12.3	9
R.G.G.	40	0.28	3.08	1.20	27.9	12

Three trends are visible. (a) As predicted by (3.5), the worst-case observer settling time scales as $1/\lambda_2(\boldsymbol{L})^{(1+\rho)/2}$; for the line graph ($\lambda_2 \sim N^{-2}$), the bound grows roughly as $N^{1.5}$, whereas for the random geometric graph (λ_2 bounded below), it grows only sublinearly. (b) The outer projected-ascent step has per-iteration complexity $O(|\mathcal{E}|)$, so its wall clock time grows linearly with the number of edges and remains in the millisecond range even for $N = 40$ on a standard laptop. (c) The per-agent communication overhead remains modest because each agent only exchanges its current observer state and command with its neighbors; densifying the graph reduces convergence time at the price of a larger neighbor count while sparsifying it shows the opposite trade-off. In practical PV plants where neighbor lists are bounded, the architecture therefore scales gracefully, and the dominant cost of large N is the slower observer rather than the cooperative optimizer.

For sparse topologies, especially line graphs, the observer settling time may exceed the four-agent coordination interval of 1.2 s used in Section 4: In Table 4 this happens for $N = 10, 20, 40$ on the line graph, and for $N = 20, 40$ on the ring. In such cases, the coordination interval must be enlarged, the observer gain k_o must be increased, or a denser communication topology (with larger $\lambda_2(\boldsymbol{L})$) must be selected so that the interarrival condition (3.33) of Theorem 3.15 remains valid. The scalability study therefore quantifies the connectivity–speed trade-off rather than claiming that the same sampling period is universally valid.

Figure 12 visualizes this trade-off and graphically validates the theoretical bound (3.5) of Theorem 3.1. The observer-time bound T_o^{bound} is plotted on a logarithmic axis as a function of N for the three topologies. The line graph follows the steepest curve, in agreement with the $N^{1.5}$ prediction; the ring grows less rapidly, and the random geometric graph remains almost flat thanks to its bounded $\lambda_2(\boldsymbol{L})$. The observed settling times (extracted from simulation, dashed lines) follow the same ordering and remain consistently below the bound, confirming that (3.5) is conservative and that the qualitative scaling law predicted by the theory is matched by the experiments.

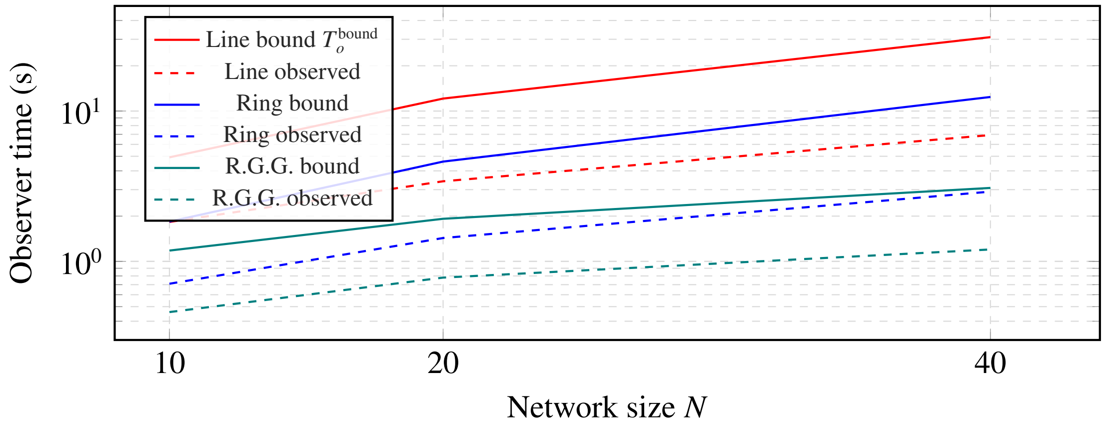

Figure 12. Observer-time bound T_o^{bound} from (3.5) (solid) and observed settling time (dashed) as a function of the network size N, for line, ring, and random geometric (R.G.G.) topologies. The line topology follows the steepest curve in agreement with the theoretical $N^{1.5}$ scaling, whereas the R.G.G. curve remains almost flat thanks to its bounded algebraic connectivity. The observed settling times remain consistently below the bound, validating the predicted scaling of Theorem 3.1.

4.6. Discussion

The simulation results confirm that every element of the proposed architecture behaves as predicted by the theory and that their combination yields a significant improvement of global power extraction. First, the observer reconstructs the sampled total power in finite time at each coordination interval with observed settling times that are smaller than the theoretical worst case. Second, the projected-ascent outer layer monotonically improves the sampled cooperative objective, satisfies the prescribed step size condition, and converges in practice to a stationary command profile, with terminal increments of order 10^{-5}. Third, the inner sliding-mode layer guarantees robust tracking of the filtered command despite the bounded uncertainty. Finally, the closed-loop architecture consistently outperforms the ANN-only, P&O, IncCond, and PSO baselines, the largest gain being recorded under the severe shading scenario. These results strongly support the practical viability of the proposed distributed finite-time coordination and tracking strategy for partially shaded PV arrays.

5. Conclusions

This paper has introduced a distributed finite-time coordination and tracking algorithm for partially shaded photovoltaic arrays. The proposed algorithm combines local ANN-based initialization, finite-time distributed reconstruction of the sampled total power, cooperative sampled-data command generation, and robust continuous-time voltage tracking. Unlike purely local MPPT methods, the developed architecture explicitly exploits interagent communication and cooperative optimization so that all PV submodules contribute to improving the harvested power under nonuniform irradiance. The overall design yields a consistent interface among distributed estimation, outer-layer coordination, and inner-loop converter control.

Three main theoretical contributions have been obtained. First, a finite-time distributed observer has been developed to reconstruct the sampled total array power from local power samples and neighbor-to-neighbor communication. Second, a regularized projected-ascent command update law has been proposed and shown to produce monotone improvement and convergence to first-order stationary points under standard smoothness. Third, a robust sliding-mode tracking law has been established for the filtered voltage commands under bounded uncertainty, ensuring finite-time reaching of the sliding manifold followed by exponential decay of the tracking error. Together, these results form an internally consistent two-time-scale distributed control framework for cooperative MPPT under partial shading.

The practical relevance of the framework has been confirmed by the simulation study: In all tested irradiance scenarios, the distributed observer converged in finite time, with settling times below the conservative theoretical bound; the outer coordination layer monotonically improved the sampled cooperative objective and reached stationary command profiles with increments of order 10^{-5}; and the inner loop quickly tracked the filtered references and preserved a clean transient behavior under irradiance changes. Most importantly, the fully coordinated architecture consistently outperformed the ANN-only baseline, with per-interval improvements of 13.1118%, 11.6677%, 16.8114%, and 12.0406%, and an average improvement of 13.4079% across the test set; it also exceeded the average power recovered by perturb and observe, incremental conductance, and PSO MPPT baselines reimplemented on the same array.

Concerning scalability, the finite-time bound (3.5) together with the empirical study in Table 4 indicates that the dominant effect of enlarging the network is the slowdown of the observer through the algebraic connectivity $\lambda_2(\boldsymbol{L})$: For sparse topologies (line), the worst-case settling time grows approximately as $N^{1.5}$, whereas for denser topologies (random geometric, small-world), it grows only sublinearly. The outer projected-ascent step retains linear-in-edges complexity, so the proposed architecture remains tractable for medium-to-large PV plants, with the practical recommendation of selecting the coordination interval as a small multiple of T_o^{bound} evaluated for the target topology.

Overall, the proposed solution shows that combining ANN-based local prediction with distributed finite-time coordination and robust tracking is a viable route to scalable PV energy management under partial shading. Future research will extend the framework toward experimental validation on a hardware platform, event-triggered and asynchronous communication schemes building on the references [24, 25] discussed in the introduction, the integration of converter efficiency and switching losses into the cooperative objective, and adaptive or fractional-order observer/controller designs for fast-varying environmental conditions.

Author contributions

O. Kahouli: Methodology, writing–original draft preparation; S. Almohaimeed: Formal analysis, supervision; L. El Amraoui: Conceptualization, software; M. Ayari: Visualization, validation; O. Naifer: Methodology, writing–original draft preparation. All authors have read and approved the final version of the manuscript for publication.

Use of Generative-AI tools declaration

The authors declare they have not used Artificial Intelligence (AI) tools in the creation of this article.

Acknowledgments

Princess Nourah bint Abdulrahman University Researchers Supporting Project number (PNURSP2026R831), Princess Nourah bint Abdulrahman University, Riyadh, Saudi Arabia.

The authors extend their appreciation to the Deanship of Scientific Research at Northern Border University, Arar, KSA for funding this research work through the project number "NBU-FPEJ-2026-2443-03".

Conflict of interest

The authors declare that they have no conflicts of interest.

References

1. A. Lashab, D. Sera, J. M. Guerrero, L. Mathe, A. Bouzid, Discrete model-predictive-control-based maximum power point tracking for PV systems: Overview and evaluation, *IEEE T. Power Electr.*, **33** (2018), 7273–7287. https://doi.org/10.1109/TPEL.2017.2764321
2. M. Y. Worku, M. A. Hassan, L. S. Maraaba, M. Shafiullah, M. R. Elkadeem, M. I. Hossain, et al., A comprehensive review of recent maximum power point tracking techniques for photovoltaic systems under partial shading, *Sustainability*, **15** (2023), 11132. https://doi.org/10.3390/su151411132
3. S. A. Sarang, M. A. Raza, M. Panhwar, M. Khan, G. Abbas, E. Touti, et al., Maximizing solar power generation through conventional and digital MPPT techniques: A comparative analysis, *Sci. Rep.*, **14** (2024), 8944. https://doi.org/10.1038/s41598-024-59776-z
4. M. H. Ali, M. Zakaria, S. El-Tawab, A comprehensive study of recent maximum power point tracking techniques for photovoltaic systems, *Sci. Rep.*, **15** (2025), 14269. https://doi.org/10.1038/s41598-025-96247-5
5. S. A. Rizzo, G. Scelba, ANN based MPPT method for rapidly variable shading conditions, *Appl. Energ.*, **145** (2015), 124–132. https://doi.org/10.1016/j.apenergy.2015.01.077
6. S. Messalti, A. G. Harrag, A. E. Loukriz, *A new neural networks MPPT controller for PV systems*, In: 2015 6th International Renewable Energy Congress (IREC), 2015, 1–6. https://doi.org/10.1109/IREC.2015.7110907
7. S. Vendoti, N. P. Tulasi, R. K. Jalli, S. Ponnuru, Z. Jin, P. Yakaiah, et al., Grid tied hybrid PV fuel cell system with energy storage and ANFIS based MPPT for smart EV charging, *Sci. Rep.*, **15** (2025), 27392. https://doi.org/10.1038/s41598-025-09626-3
8. A. F. Megri, H. Bayarassou, New predictive control for maximum power point tracking technique based on fuzzy dynamic programming, *Electr. Eng.*, **107** (2025), 11667–11682. https://doi.org/10.1007/s00202-025-03114-7
9. M. Y. M. Aldulaimi, M. Çevik, AI-enhanced MPPT control for grid-connected photovoltaic systems using ANFIS-PSO optimization, *Electronics*, **14** (2025), 2649. https://doi.org/10.3390/electronics14132649

10. R. B. Salah, O. Kahouli, H. Hadjabdallah, A nonlinear Takagi-Sugeno fuzzy logic control for single machine power system, *Int. J. Adv. Manuf. Technol.*, **90** (2017), 575–590. https://doi.org/10.1007/s00170-016-9351-4

11. A. Kahouli, T. Guesmi, H. H. Abdallah, A. Ouali, *A genetic algorithm PSS and AVR controller for electrical power system stability*, In: 2009 IEEE 6th International Multi-Conference on Systems, Signals & Devices (SSD), 2009, 1–6. https://doi.org/10.1109/SSD.2009.4956736

12. B. Dhouib, Z. Alaas, O. Kahouli, H. H. Abdallah, Determination of optimal location of FACTS device to improve integration rate of wind energy in presence of MBPSS regulator, *IET Renew. Power Gen.*, **14** (2020), 3526–3540. https://doi.org/10.1049/iet-rpg.2020.0679

13. F. M. De Oliveira, M. H. M. Brandt, F. Salvadori, J. E. E. Izquierdo, M. R. Cavallari, O. H. A. Junior, Development of an MPPT-based genetic algorithm for photovoltaic systems versus classical MPPT techniques in scenarios with partial shading, *Inventions*, **9** (2024), 64. https://doi.org/10.3390/inventions9030064

14. A. Fathy, A new arrangement methodology for enhancing PV array production under partial shade operation, *Energy*, **346** (2026), 140190. https://doi.org/10.1016/j.energy.2026.140190

15. N. G. Poothullil, A. Saleem, Pandiagonal magic square reconfiguration of partially shaded photovoltaic arrays for simplified MPPT and power enhancement, *IEEE Access*, **14** (2026), 23194–23210. https://doi.org/10.1109/ACCESS.2026.3661978

16. L. Moussaoui, F. Merahi, A simple physical string arrangement reconfiguration (PSAR) for enhanced energy production in partially shaded PV arrays, *Adv. Electr. Comput. Eng.*, **26** (2026), 105–114. https://doi.org/10.4316/AECE.2026.01011

17. P. Murugesan, P. W. David, P. K. Balachandran, M. A. A. M. Zainuri, Optimal Battery-based adaptive reconfiguration technique for a partially shaded photovoltaic array, *Energy Sci. Eng.*, **14** (2026), 99–128. https://doi.org/10.1002/ese3.70340

18. N. A. Samee, F. Ahmed, M. A. Mahdy, M. Alabdulhafith, E. H. Houssein, A novel improved puma optimizer to boost photovoltaic array production in partially shaded environments, *Comput. Model. Eng. Sci.*, **146** (2026). https://doi.org/10.32604/cmes.2025.069931

19. D. C. Nautiyal, H. S. Sahu, S. Tripathi, M. K. Mishra, S. K. Nayak, A novel PLI technique for maximum power estimation of a partially shaded PV array, *IEEE T. Ind. Inform.*, **22** (2026), 3495–3506. https://doi.org/10.1109/TII.2025.3649604

20. B. B. Pathik, N. Amin, S. J. Rahman, *A comprehensive review on mitigating partial shading in photovoltaic systems*, In: 2026 5th International Conference on Electrical, Computer & Telecommunication Engineering (ICECTE), 2026, 1–6. https://doi.org/10.1109/ICECTE69292.2026.11429226

21. H. G. Sezgin-Ugranlı, From conventional designs to advanced approaches of bypass diode utilization in PV systems, *Renew. Sust. Energ. Rev.*, **229** (2026), 116657. https://doi.org/10.1016/j.rser.2025.116657

22. F. Guo, C. Wen, J. Mao, Y. D. Song, Distributed secondary voltage and frequency restoration control of droop-controlled inverter-based microgrids, *IEEE T. Ind. Electron.*, **62** (2015), 4355–4364. https://doi.org/10.1109/TIE.2014.2379211

23. S. M. Rostami, M. Hamzeh, H. Nazaripouya, Distributed cooperative reactive power control of PV systems with dynamic leader, *IEEE T. Ind. Inform.*, **20** (2024), 8972–8982. https://doi.org/10.1109/TII.2024.3372615

24. Z. Sajjadinezhad, N. M. Dehkordi, Fully distributed adaptive event-triggered control with delay-aware dynamic thresholds for islanded AC microgrids, *Sci. Rep.*, **15** (2025), 27900. https://doi.org/10.1038/s41598-025-13955-8

25. O. Lopez-Santos, M. Merchán-Riveros, G. Garcia, *Event-triggered digital implementation of MPPT for integration of PV generators in DC buses of microgrids*, In: Communications in Computer and Information Science, vol 915. Springer, Cham, 2018. https://doi.org/10.1007/978-3-030-00350-0_45

26. S. Li, X. Wang, Finite-time consensus and collision avoidance control algorithms for multiple AUVs, *Automatica*, **49** (2013), 3359–3367. https://doi.org/10.1016/j.automatica.2013.08.003

27. M. Iqbal, P. Kolios, M. M. Polycarpou, Finite-and fixed-time consensus protocols for multi-agent systems with time-varying topologies, *IEEE Contr. Syst. Lett.*, **6** (2022), 1568–1573. https://doi.org/10.1109/LCSYS.2021.3124938

28. V. Utkin, J. Guldner, J. Shi, *Sliding mode control in electro-mechanical systems*, 2 Eds., CRC Press, 2009.

29. C. Edwards, S. K. Spurgeon, *Sliding mode control: Theory and applications*, Taylor & Francis / CRC Press, 1998. https://doi.org/10.1201/9781498701822

30. E. B. Alaia, S. Dhahri, O. Naifar, Adaptive observer design with fixed-time convergence, online disturbance learning, and low-conservatism linear matrix inequalities for time-varying perturbed systems, *Math. Comput. Appl.*, **30** (2025), 112. https://doi.org/10.20944/preprints202508.1524.v1

31. O. Naifar, *Practical observer design for nonlinear systems using caputo fractional derivative with respect to another function*, In: 2025 IEEE 22nd International Multi-Conference on Systems, Signals & Devices (SSD), 2025, 411–418. https://doi.org/10.1109/SSD64182.2025.10989893

AIMS Press